Advances in measuring multiply-substituted isotopologues of gas molecules with geochemical applications

Edward D Young[a], Jabrane Labidi[b], and Issaku E Kohl[c], [a]Department of Earth, Planetary, and Space Sciences, UCLA, Los Angeles, CA, United States; [b]Université de Paris Cité, Institut de physique du globe de Paris, CNRS, Paris, France; [c]Department of Geology & Geophysics, University of Utah, Salt Lake City, UT, United States

© 2024 Elsevier Inc. All rights are reserved, including those for text and data mining, AI training, and similar technologies.

Introduction 2
High-mass-resolution gas-source isotope ratio mass spectrometry (HR-IRMS) 3
Mass resolving power 3
Double focusing IRMS 5
Large geometry IRMS 5
High-mass-resolution as a diagnostic tool 6
Example applications 8
CH_4 8
CH_3 11
N_2 12
O_2 14
H_2 15
N_2O 15
Orbitrap Fourier-transform IRMS 16
Science motivation 16
Principles of hybrid Orbitrap mass analysis 17
Acquiring isotopologue information from a Hybrid Orbitrap MS 18
Considerations for designing measurement approaches 18
Sensitivity 18
Resolution and signal to noise 19
Fragmentation 19
Example applications 20
Electron impact source sample introduction 21
Electrospray liquid sample introduction 21
Summary and outlook 22
References 23

Abstract

Recent advances in gas-source isotope ratio mass spectrometry (IRMS) have enabled access to previously inaccessible information contained in the distribution of isotopes among gas molecules of geochemical interest. Increases in mass resolution afforded by incorporation of double focusing and larger magnetic sectors removes many limitations imposed by mass interferences. At the same time, new Fourier transform mass spectrometry applications afford leaps of an order of magnitude in mass resolution, providing access to position-specific isotope ratios in larger molecules. Applications of these new technologies have led to studies of clumped isotopes in CH_4, CH_3, N_2, O_2, H_2, and N_2O, among other molecules in the laboratory and in natural settings. These studies comprise a bevy of new geochemical tracers spanning diverse fields from biogeochemistry to volcanology, marine geochemistry to atmospheric chemistry, and cosmochemistry.

Keywords

Isotope clumping; Electrostatic sector analyzer; Fourier-transform ion cyclotron mass spectrometry; High-resolution isotope ratio mass spectrometry; Isotopologue; Nuclear Magnetic Resonance (NMR)

Key points

- Describe advancements in isotope ratio mass spectrometry of gases with geochemical applicability;
- Review recent progress in measuring rare isotopologues ("clumped isotopes") of geochemically relevant gas molecules through the lens of advancements in instrumentation;
- Provide examples of discoveries made with these new tools.

Introduction

The term "rare isotopologue" (see footnote) refers to molecules composed of more than one rare isotope. Their usefulness lies in the fact that their distribution is an intra-phase or intra-molecular isotope signal that can be read without reference to any other species; normally, stable isotope ratios for a phase or molecule are interpretable only when compared with ratios in another phase or molecule. Rare isotopologues therefore offer great utility in extraterrestrial settings where isotope ratio measurements are likely to be made in isolation without the benefit of the full context that is available in terrestrial settings.

Investigations into the phenomenon of multiple rare isotope substitution dates back to the use of isotopes in general (e.g., Lewis and Cornish, 1933). In the geochemical literature, Richet et al. (1977) presented a useful illustration of the temperature-dependence of the relative abundances of multiply-substituted isotopologues. Using the "internal" reaction $H_2O + D_2O \rightleftharpoons 2HDO$ as an example, these authors showed how the equilibrium constant rises with temperature as D_2O becomes less favored. They further showed that the equilibrium constant is asymptotic to the ratio of reactant symmetry numbers (subscript r) divided by product symmetry numbers (subscript p) with increasing temperature, as mandated by the Pauli exclusion principle, so that in this example,

$$\lim_{T\to\infty} k_{\mathrm{Eq}} = \frac{\prod_r \sigma_r}{\prod_p \sigma_p} = \frac{2\times 2}{1\times 1} = 4. \tag{1}$$

More recently, multiply-substituted isotopologues have been explored extensively as tracers in the geosciences where they are colloquially referred to as possessing "isotope clumping." Most prominent in this context has been applications involving CO_2 (Eiler and Schauble, 2004; Wang et al., 2004) and the related intra-mineral geochemical thermometer afforded by isotope clumping in CO_2 extracted from carbonate minerals by acid digestion (Eiler et al., 2005; Gosh et al., 2004). Applications to molecules other than CO_2 required advancements in gas-source mass spectrometry, the subject of this chapter.

A gas molecule containing a "clump" of two heavy, stable isotopes is more thermodynamically stable than molecules containing a single heavy isotope because of the reduction in vibrational frequencies, ν, afforded by the presence of two heavy isotopes bonded together; $\nu \propto \mu^{-1/2}$ where μ, the reduced mass, is larger for the bonds involving heavy isotopes. The decreases in vibrational frequencies, and thus energy, are most influential at lower temperatures so that the clumping of heavy isotopes is temperature dependent. For example, $^{13}C^{16}O^{18}O$ is slightly more stable at low temperatures than $^{12}C^{16}O^{18}O$ (Wang et al., 2004; Eiler and Schauble, 2004). With falling temperature, the small enhancement in stability results in increasing abundances of the multiply substituted isotopologue relative to the purely stochastic distribution of isotopes among the molecules expected at high temperatures (e.g., Eq. 1). If isotopic equilibration is not attained, kinetic isotope fractionation of clumped isotopologues may yield signatures diagnostic of specific reaction mechanisms (Wang et al., 2004; Eiler, 2007).

Eiler and co-workers recognized that a conventional, low-mass-resolution gas-source mass spectrometer was capable of resolving the rare isotopologue $^{13}C^{16}O^{18}O$ (integer mass of 47)[1] and successfully executed the first calibrated study of doubly-substituted CO_2 molecules in natural terrestrial samples (Eiler and Schauble, 2004; Wang et al., 2004; Ghosh et al., 2006a,b; Schauble et al., 2006; Affek and Eiler, 2006; Affek et al., 2008; Affek and Xu, 2007; Ghosh et al., 2007; Guo and Eiler, 2007). The enhanced thermodynamic stability of gas molecules composed of two heavy, rare isotopes was exploited to calibrate experimentally a gas formation thermometer. A striking result is that CO_2 produced by respiration can be distinguished from that produced by combustion by measuring the relative abundance of $^{13}C^{16}O^{18}O$ (Affek and Eiler, 2006).

Following up on this work, the method was extended to include CO_2 released from carbonate minerals. This resulted in a widely used intra-mineral thermometer based on Δ_{47}, the concentration of the mass-47 isotopologue of CO_2 released by phosphoric acid digestion of carbonate minerals. The method works because carbon-oxygen isotope clumping in the CO_3^{--} moiety is largely preserved even after acid digestion. The Δ_{47} values are per mil deviations in the relative concentration of $^{13}C^{16}O^{18}O$ relative to the stochastic distribution in which carbon and oxygen isotopes are distributed randomly over all CO_2 isotopologues in a gas sample. In these applications, a calibration is made between the concentration of mass-63 CO_3 ions in the carbonate structure relative to stochastic ($^{13}C^{16}O^{16}O^{18}O$ and its isotopic isomers, expressed as Δ_{63}) and the measured Δ_{47} values of the extracted carbon dioxide gas. In effect, empirical functions relating measured Δ_{47} values to carbonate formation temperatures are obtained through rigorous experiment. The challenges to precise and accurate measurements of Δ_{47} values in CO_2 are the low measured ion currents associated with $^{13}C^{16}O^{18}O^+$, encroaching on the limits imposed by random fluctuations of current in Faraday cup RC amplifiers (shot noise, see Petersen et al., 2019) and baseline variations caused by scattering of electrons and ions across all collectors (Petrizzo and Young, 2014; Yeung et al., 2018; He et al., 2012).

Recently, improvements in amplifier gains for Faraday collectors (use of $10^{13}\Omega$ resistors) have allowed measurements of the concentrations of $^{12}C^{18}O^{18}O$ relative to stochastic values (expressed as per mil deviations from the stochastic distribution, Δ_{48}) (Fiebig et al., 2019). Thermodynamic equilibrium should yield concordant temperatures using Δ_{47} and Δ_{48}. When the CO_2 is obtained by acid digestion of carbonate, Δ_{47} and Δ_{48} represent the concentrations of $^{13}C^{16}O^{16}O^{18}O$ and $^{13}C^{16}O^{18}O^{18}O$ in the carbonate CO_3^{--} relative to stochastic, expressed as Δ_{63} and Δ_{64}, respectively. Discordant temperatures from these two thermometers

[1]We will use the terms "isotopologue" and "isotopomer" as defined by the IUPAC. An isotopologue is defined as a molecular entity that differs only in isotopic composition (number of isotopic substitutions), e.g., $^{13}CH_4$, $^{13}CH_3D$, and $^{12}CH_2D^2$. In the example of methane, $^{13}CH_4$ is a "singly substituted" isotopologue and $^{13}CH_3D$ is a "doubly substituted" isotopologue. Singly substituted isotopologues are more abundant compared to rare, doubly substituted isotopologues in natural systems. An isotopomer is an isomer having the same number of each isotope but differing in their positions. The term is a contraction of "isotopic isomer." Simple examples are $C^{18}O^{16}O$ and $C^{16}O^{18}O$.

indicate kinetic effects are present, invalidating temperature estimates based on the assumption of thermodynamic equilibrium (Bajnai et al., 2020; Lucarelli et al., 2023).

The success of the CO_2 work and the myriad ensuing applications of the clumped-isotope carbonate thermometer served to draw attention to a number of potential "clumped isotope" thermometers, generating interest in a broad range of potential new applications involving different gas molecular species. However, it was soon realized that moving beyond CO_2 was going to require instruments with greater mass resolution. For example, in the case of methane, $^{13}CH_3D$ and $^{12}CH_2D_2$ both have integer mass 18. Therefore, resolving their actual masses of 18.04094 and 18.04386, respectively, requires measurements with mass spectrometers capable of greater mass resolution than has been customary in the field. While high-mass resolution instruments for isotope ratio analysis were available for secondary ionization mass spectrometry (SIMS) and multiple-collector inductively-coupled plasma-source mass spectrometry (MC-ICPMS), gas-source isotope ratio mass spectrometers (referred to as IRMS instruments) were universally smaller in geometry with limited resolution. Recent development of higher-resolution gas-source IRMS instruments, as well as spectroscopic methods, has been essential to developing "clumped isotopes" for O_2 (Yeung et al., 2012, 2015, 2016; Laskar et al., 2019), CH_4 (Ono et al., 2014; Stolper et al., 2014; Wang et al., 2015; Young et al., 2016, 2017), CH_3 (Lloyd et al., 2021, 2023), higher-order hydro-carbon molecules (e.g., Clog et al., 2018; Taguchi et al., 2022), N_2 (Yeung et al., 2017, 2019; Labidi et al., 2020; Labidi and Young, 2022), H_2 (Popa et al., 2019; Mangenot et al., 2023), and N_2O (Magyar et al., 2016). At the same time, new Fourier transform IRMS applications afford leaps in mass resolution that greatly enhance the isotope information content of gas molecules, organic molecules, and molecular ions dissolved in solution (Eiler, 2007; Eiler et al., 2020; Neubauer et al., 2018; Hilkert et al., 2021; Mueller et al., 2022).

High-mass-resolution gas-source isotope ratio mass spectrometry (HR-IRMS)

Mass resolving power

Stable isotope geochemists, cosmochemists, and atmospheric scientists were, until about 10 years prior to this writing, using gas-source mass spectrometers that had scarcely changed at all in mass resolving power since the 1950s. The innovative designs of Nier, McKinney, Thode, and others that inaugurated the study of light stable isotopes in nature typically operated with a magnetic sector of 6-in. radius of curvature, not very different from many currently available instruments (Nier, 1947; McKinney et al., 1950). A crucial advantage of these gas-source instruments is the exploitation of rapid switching between sample and standard gases, the so-called "dual inlet" design, to account for instrumental mass fractionation effects. Mass spectrometers based on these early design principles remain successful at the present time. Gas-source, electron-impact, magnetic sector instruments for the analysis of light stable isotopes (IRMS instruments) have been updated with more collectors, turbo-molecular pumps, helium carrier gas with differential pumping, digital electronics, and computer automation, but mass resolution was scarcely changed. The integer-mass ion beams of, for example, H_2^+, O_2^+, CO_2^+, SO_2^+, and SF_5^+ and their singly substituted isotopologue equivalents are all resolved sufficiently well by the classical instruments to permit high-precision measurement of bulk isotope ratios in these gases. But many important analytical targets, especially molecules containing more than one rare isotope plagued by mass interferences from isobaric molecular and atomic species with the same integer masses, remained inaccessible.

Magnetic sector mass spectrometers rely on the difference in radius of the curved beam path through the magnetic field, according to the equation

$$r = \sqrt{\frac{2mV}{zB^2}}, \tag{2}$$

where r is the radius of the path, m is the mass of the ion, z is the charge on the ion, and V is the accelerating voltage propelling the ion through the magnetic field B. The minimum mass difference that can be resolved by a mass spectrometer depends on the width of the ion beam image at the collectors, i, compared with the dispersion D (Fig. 1). Dispersion refers to the distance between the highest and lowest masses that can pass through the instrument to reach the collectors. The mass resolving power (MRP) is then the number of ion beam images that fit on the dispersion plane (focal plane). That is to say, $\mathrm{MRP} = D/i$. The dispersion is a function of the radius of the magnetic sector (Fig. 1). For unit magnification (e.g., the ratio of the length of incident ion beam path to the magnet and the length of ion beam paths from the magnet), dispersion D is approximately equal to 2 times the radius of the magnetic sector R as a result of stigmatic focussing (Cross, 1951). Therefore, larger instruments with a larger radius R have greater mass resolving power, all else equal, and a greater capacity to separate ions with small differences in mass. We note that the image width i is equal to $Xs + a$, where s is the object width defined by the entrance slit to the instrument (Fig. 1), a is broadening at the collector end due to aberrations, and X is the image magnification. Simply magnifying D by lengthening the path from the magnet to the detectors does not improve mass resolving power, to first order, since in this case $\mathrm{MRP} = 2RX/(Xs + a) \sim 2R/s$, ignoring aberrations, showing that magnification X cancels. Improvements in resolution come from modifications that result in reduction of aberrations and greater values of D/X (Matsuda, 1990).

A history of the evolution of magnetic-sector mass spectrometers in terms of their dispersion/image magnification, D/X, is presented in Fig. 2. The advances in mass resolution afforded by the new IRMS instruments has resulted in a wealth of new science reliant on measuring isotopologues of various gas species. We summarize just a few of these applications in what follows.

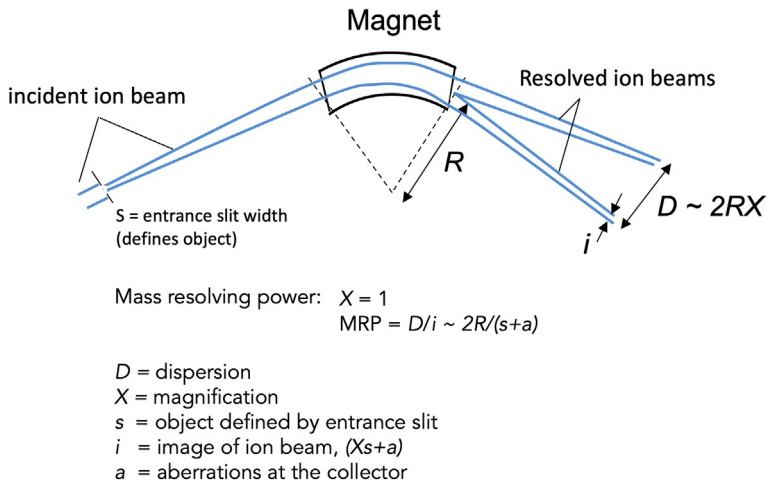

Fig. 1 Basic geometry of a magnetic sector mass spectrometer, illustrating the concept of mass resolving power. The mass resolving power (MRP) is the number of beams of width $\sim i$ that fit on the focal plane with dispersion D. D depends on the radius of the magnet, R.

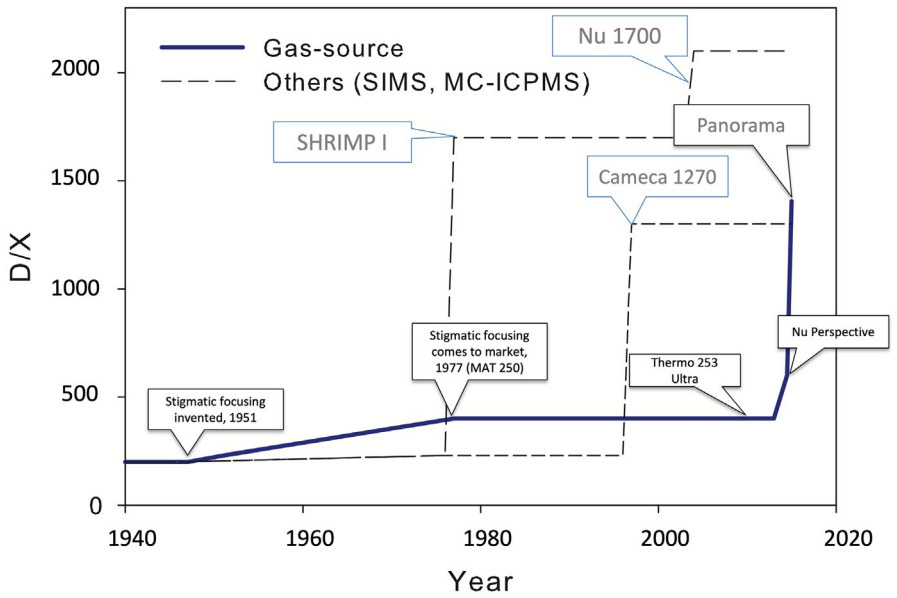

Fig. 2 A simplified history of the evolution of magnetic-sector, isotope-ratio mass spectrometers in terms of their dispersion relative to image magnification, D/X. The dashed lines refer to non-gas-source instruments, and the solid line refers to gas-source instruments generally used for light stable isotopic analysis of gases.

The mass resolving power of an instrument is a measure of the steepness of the peak shape. Peak shape in mass spectrometry is the shape of the ion beam signal obtained as the beam is swept across the collector. The width of the limbs of the peaks during the scanning are a measure of the width of the ion beam. Flat top peak shapes are desired to minimize the effects of instrumental drift. Flat tops require collector apertures $\geq$3 times the width of the ion beam at the collector (Fig. 3). It is worth pointing out here that mass resolution is not synonymous with mass resolving power (MRP), although the two are related. Mass resolution (MR) generally refers to $m/\Delta m$ where m is mass and Δm is the difference in mass that is well resolved using flat-top peaks (the definitions of "well resolved" vary from application to application). Mass resolution depends on the setup of the instrument, including the widths of collector slits, for example, while MRP is a measure of the instrument geometry (dispersion and entrance slit width, inclusive of aberrations). MR is thus often cited when describing an analytical setup, while MRP is used to describe the performance of the instrument more generally. Because flat-top peak shapes require ion beams to be at least several times narrower than the collector aperture, a useful approximation is that MR is $\leq$MRP/3 (e.g., an MR of 10,000 would correspond to an MRP of at least 30,000).

Classical gas-source IRMS instruments have a mass resolving powers $\leq$1, 000 based on $R \leq 250$ mm, $i \sim 0.5$ mm and magnification of 1. However, there are no fundamental barriers to achieving high mass resolving power in gas-source mass spectrometry in general, and high mass resolution is applied routinely in other applications of mass spectrometry. High-resolution mass

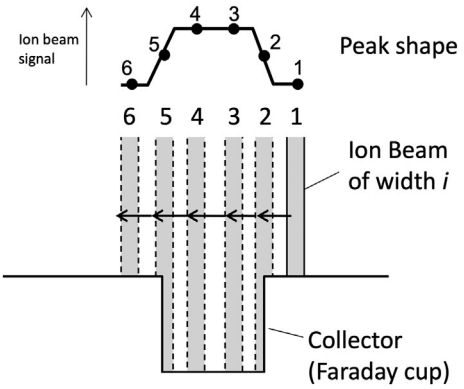

Fig. 3 Illustration of the meaning of the term "peak shape". Here the points 1 through 6 refer to six different positions of an ion beam incident on a collector (e.g., a Faraday cup). Position (x axis here) can be expressed in terms of magnet current or, for convenience, corresponding mass/charge. Ion beams narrower than the aperture of the collector result in flat-top peak shapes as the magnetic field is varied and the beams are scanned across the collector.

spectrometry is a necessary part of stable isotope analysis in SIMS (Secondary-Ion Mass Spectrometer) and MC-ICPMS (Multi-Collector Inductively Coupled Plasma-source Mass Spectrometer) techniques. SIMS analysis is plagued by the formation of hydrides, among other interfering species. MC-ICPMS measurements encounter molecular species, often produced in the plasma itself, that interfere with analyte signals. Examples include $^{16}OH^-$ interfering with $^{17}O^-$ in SIMS and $^{16}O^{40}Ar^+$ interfering with $^{56}Fe^+$ in MC-ICPMS. Both of these interferences are eliminated routinely by high mass resolving power. Values for MRP in these applications are generally $\geq$10,000.

The spread in energy of ions incident on the magnetic sector will limit mass resolution. Variations in kinetic energy result in smearing of the image of the entrance slit at the collectors as the beams pass through the magnetic sector with spread in velocities. An energy sector is therefore required before the magnetic sector to achieve high MRP. An electrostatic sector analyzer (ESA) separates ions according to the radius of their path as a function of their kinetic energy, according to equation $r = 2E_{\text{kinetic}}/(zE_{\text{field}})$ where $E_{\text{kinetic}} = 1/2mv^2$ is the kinetic energy of the ion with velocity v and E_{field} is the electrostatic field perpendicular to the path. So-called double focusing instruments, with both an electrostatic sector analyzer (ESA) and a mass analyzer, date back to Dempster (1935). With few exceptions (Johnson and Nier, 1953; Nier, 1953), however, double-focusing gas-source IRMS instruments have been exceedingly rare until recently.

Double focusing IRMS

The stagnation in IRMS design broke in 2013, when Thermo Scientific introduced a double-focusing gas-source IRMS instrument based on their MC-ICPMS platform (Eiler et al., 2013), called the 253 Ultra™. This gas-source IRMS has a standard magnetic sector with $R = 230$ mm, but when combined with the improvement in peak shape afforded by its ESA (Fig. 4) and a narrow entrance slit, it is capable of operating with maximum MRP values of up to about 50, 000. This is sufficient for many clumped isotope applications.

Large geometry IRMS

While mass resolution, or MRP, is essential for many rare isotopologue ratio measurements due to the numerous mass interferences, sensitivity at high mass resolution is equally important. From the formula for MRP $= D/i$ it is clear that a smaller entrance slit width i affords higher resolution, but it does so at the cost of less signal (narrow slit cuts out much of the ion beam produced in the source). The solution is to build mass spectrometers with larger radii (i.e., greater dispersion D) within practical limitations of controlling the ion optics. Methane is a good example of the limitations that low abundances can impose on signal intensity. The relative abundance of the $^{12}CH_2D_2$ isotopologue is 1.45×10^{-7}, compared with the relative abundance of the singly-substituted isotopologue $^{13}CH_4$ of 1.1×10^{-2}. This means for normal conditions, while the major ion and the singly-substituted ions are measured with Faraday cups and amplifiers, the $^{12}CH_2D_2^+$ ion beam must be measured with an ion counter (e.g., a secondary electron multiplier) at relatively low count rates. In general, the larger the radius, the more signal one can obtain at a given mass resolution. In practice, entrance slit widths less than about 5 μm yield signals that are too small for useful isotopologue ratio measurements, and slit widths of perhaps 15 to 35 μ m are preferable for high transmission at high mass resolution.

Design considerations for high-mass-resolution gas-source IRMS instruments, or for any isotope ratio mass spectrometer for that matter, therefore must trade off MRP with sensitivity. Again using methane as the example, the $m/\Delta m$ defined by the two mass-18 isotopologues $^{13}CH_3D$ and $^{12}CH_2D_2$ is 6178. In most applications one finds that a useful separation between two overlapping masses requires an MRP that is $\sim$5$\times$ the $m/\Delta m$ defined by the masses, indicating that measurements that separate these two isotopologues require an MRP of at least 30, 000. Using MRP $= D/i$ and an entrance slit width i of 35 μm suggests that the radius of

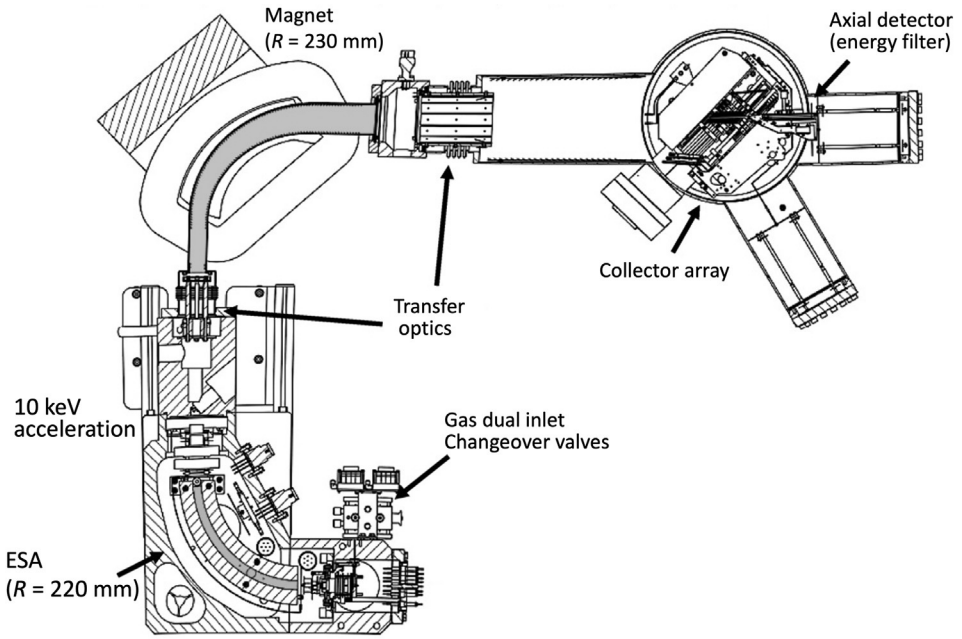

Fig. 4 Layout of the Thermo Fisher Scientific 253 Ultra™ high-mass-resolution IRMS instrument (Eiler et al., 2013).

the magnetic sector, R, for an instrument to be used for this purpose should be of order 525 mm or more (this is a minimum value that excludes aberrations), twice that which is typical of most standard IRMS instruments.

Matsuda (1974) calculated that aberrations in double focusing mass spectrometers are minimized using a combination of an ESA followed by a large quadrupole electrostatic lens, and then a magnetic sector. This "Matsuda optics" design was the basis for the early high-mass-resolution SIMS instrument (the SHRIMP, Ireland, 2014). In 2014, Nu Instruments introduced a proto-type large-geometry IRMS named the Panorama™ that was built expressly to address the problem of high mass resolution coupled with high sensitivity. Its design is based on the Matusda optics (Young et al., 2016). This instrument combines a 1017.6 mm radius ESA with a 800 mm-radius magnetic sector (Fig. 5). Between the ESA and magnet is a large quadrupole lens that minimizes aberrations and improves vertical focusing. The instrument also includes continuously variable collector slits, enabling screening out of mass interferences on both sides of a target analyte mass/charge peak.

The 253 Ultra was the first commercial high-mass-resolution gas-source IRMS, and the Panorama was the first large-geometry gas-source high-mass-resolution IRMS. We refer to both, and their descendants, as HR-IRMS instruments. The Panorama has a total ion path length of 6.2 m, a dispersion of 630 mm by virtue of the radius and a magnification of 0.448. Operation at an MRP of 40,000 to 60,000 is routine, and a maximum useful MRP of 80,000 has been easily achieved. MRP is measured as $M/\Delta M$ where M is mass over charge for the ion beam and ΔM is the 5%–95% definition of beam width in mass-to-charge units (Fig. 6). The MRP of 40,000 corresponds to an effective source slit width, s, of 35 μm using $\mathrm{MRP} = D/(Xs)$ where X is the magnification. With this slit width, the large geometry allows for MRPs of ~40,000 with only a modest reduction in transmission (sensitivity) of order 4×. The relationship between MRP and mass resolution, MR, is illustrated in Fig. 6. The peak-to-peak mass/charge difference used to define mass resolution is similar to that defined by the widths of the peak shapes in m/z as defined at 10% ion current (a commonly used measure of MR). The widths of the peak shapes are controlled by the collector slit widths. Where an analyte is bracketed by interfering ion beams (as in Fig. 6), MR becomes especially relevant, illustrating the usefulness of collector slits of appropriately narrow widths. By using narrow collector slits, mass/charge interferences on both sides of the analyte peak can be minimized, if not eliminated.

A peak-shape plot for methane integer masses 16, 17, and 18 (in this case, $^{12}CH_2D_2{}^+$) obtained using the large-geometry HR-IRMS instrument (prototype Panorama at UCLA) is shown in Fig. 7. The plot illustrates that, in addition to the $^{12}CH_2D_2{}^+$ mass-18 beam being base-line resolved from the $^{13}CH_3D^+$ mass-18 beam (the latter ion beam is far beyond the low-mass limit of the plot), $^{12}CH_2D_2{}^+$ is also resolved from mass interferences from $^{13}CH_5^+$ and $^{12}CH_4D^+$, both created by ion-molecule reactions in the electron impact (EI) source.

High-mass-resolution as a diagnostic tool

The high mass resolution afforded by the new class of HR-IRMS instruments is useful for diagnosing analytical artifacts that arise on lower-resolution, classical instruments. We illustrate this with some observations regarding baselines.

Recent work indicates that measurements of doubly-substituted (clumped) isotopologues of O_2 ($m/z = 36$) and CO_2 ($m/z = 47$) on classical IRMS instruments suffer from negative displacements in baselines that exist only when ion beams are present in the

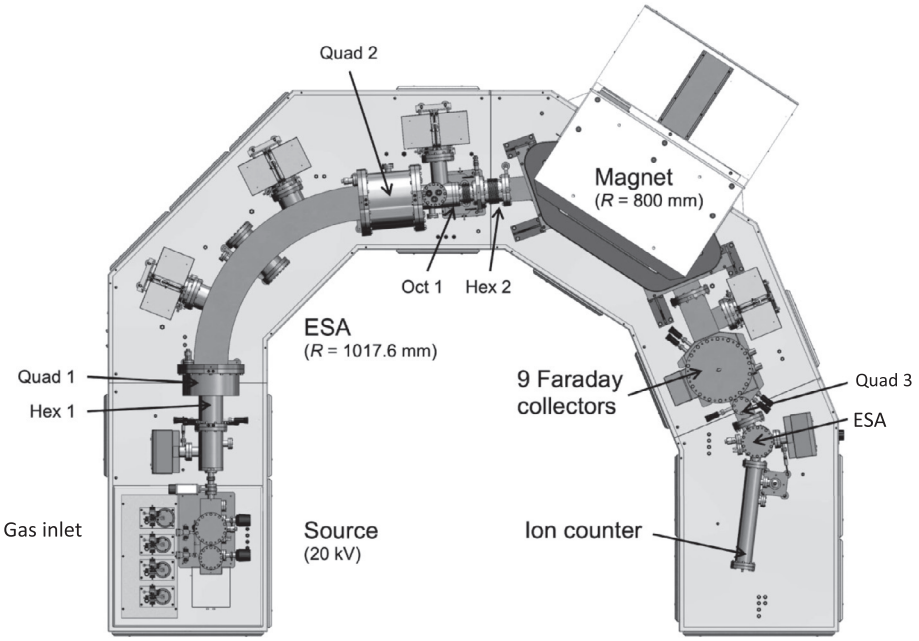

Fig. 5 Layout of the Nu Instruments Panorama™ large-geometry IRMS instrument (Young et al., 2016).

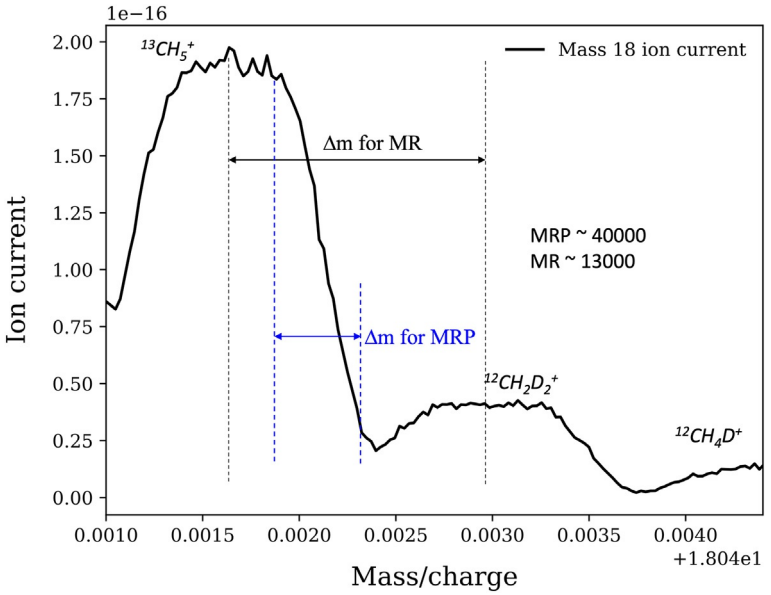

Fig. 6 Illustration of the difference between mass resolving power (MRP) and mass resolution (MR) using $^{12}CH_2D_2{}^+$ and adjacent interfering ion beam using the Panorama high-mass-resolution IRMS at UCLA. Ion current values refer to conversion of counts per second to amps. For comparison to the mass resolution (MR) of ~13,000 and the mass resolving power (MRP) of ~40,0000 shown here, the $m/\Delta m$ between $^{12}CH_2D_2^+$ and $^{13}CH_5^+$ is 13,100 and that between $^{12}CH_2D_2^+$ and $^{12}CH_4D^+$ is 11,700. Figure modified from Young ED, Rumble D, Freedman P, and Mills M (2016) A large-radius high-mass-resolution multiple-collector isotope ratio mass spectrometer for analysis of rare isotopologues of O2, N2, CH4 and other gases. *International Journal of Mass Spectrometry* 401: 1–10.

collectors (Yeung et al., 2012, 2018; He et al., 2012). These "pressure baselines" are the source of analytical error at the tens of ppm level if not accounted for, and are presumed to be a general effect, but with the details varying with instrument and conditions. The source of the baseline depression is thought to be sprays of secondary electrons caused by ion beams striking metal in the vicinity of the Faraday collectors (Yeung et al., 2012). The ability to vary collector slit widths at high mass resolution permits one to investigate the validity of the pressure baseline correction schemes.

Fig. 8 illustrates the lowering of the $^{17}O^{16}O^+$ ion beam(mass-33) baseline by secondary electrons produced by the $^{16}O^{16}O^+$ ion beam (mass-32) when measuring O_2 using an HR-IRMS (in this case, the Panorama prototype). By widening the collector slits for

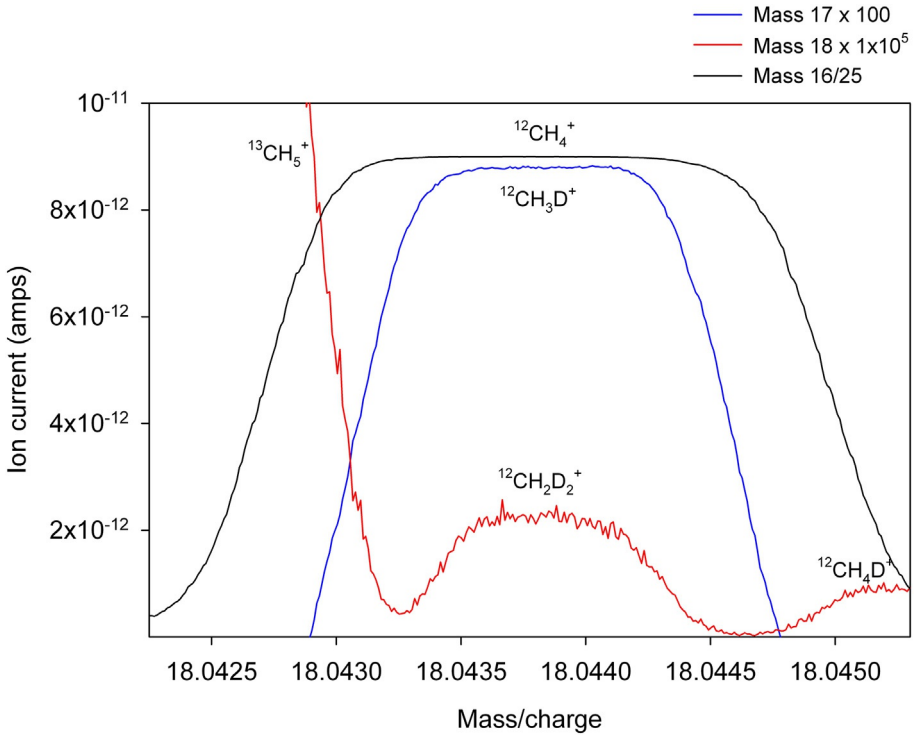

Fig. 7 Methane peak shapes for $^{13}CH_4^+$, $^{13}CH_3D^+$, and $^{12}CH_2D_2{}^+$ obtained using the Panorama HR-IRMS prototype. The $^{13}CH_3D^+$ beam is seen to be resolved from mass interferences from $^{13}CH_5^+$ and $^{12}CH_4D^+$, both created by ion-molecule reactions in the electron impact source. Ion current values on the ordinate refer to conversion of counts per second for the mass-18 collector to amps and then scaled as indicated.

the mass-32 beam, one can see that lowering of the baseline for mass-33 occurs when the mass-32 beam is outside of its Faraday collector. The ramps in the mass-33 baselines on either side of the main peak track the edges of the mass-32 peak perfectly, as can be shown by moving the mass-32 slits. The correlation between the reduction in the background ion current for mass-33 and the degree to which the 32 beam is out of its Faraday collector calls into question the validity of pressure baseline corrections as currently implemented. When the mass-32 ion beam is in its Faraday collector, the secondary electrons spray produced by its impacting metal (e.g., the slit assembly) is greatly reduced. The depression in the mass-33 baseline is thus not the correct background to use for a measurement because when the beams are aligned in their collectors, the source of the baseline depression (secondary electrons) is not present (or is greatly reduced). The apparent pressure baseline is an "edge" effect, an artifact of producing an excess of secondary electrons as the beams are scanning across the edges of the entrances to the cups. Because the ion beams are generally of similar width in classical, low-mass-resolution instruments, the "edge" effect of electron spray appears on the flanks of all of the peak shapes (e.g., He et al., 2012), in proportion to the sensitivity of the amplifiers, disguising the fact that this baseline depression will not be present when the magnet and accelerating voltage center the beams in their respective cups. In any event, several manufacturers now offer energy filters adjacent the Faraday collectors that eliminate observable deflections in baselines on the smaller instruments.

Example applications

CH_4

Tracing the origins of methane gas is important for our understanding of global climate change, the future of natural gas as an energy source, and links between the two. Newly developed markers for chemical pathways for methane formation have potential applications elsewhere in the Solar System as well. In the last decade, several groups have begun to make use of the rare, doubly-substituted mass-18 isotopologues of methane gas as tracers of provenance. Early, there was a focus on using the relative abundance of $^{13}CH_3D$ as a thermometer, by analogy with CO_2. Generally, microbial methanogenesis (microbialgenesis) is thought to generate methane at temperatures <90 °C, thermogenic gases are produced at temperatures of >120 °C, and abiotic methane can evolve from reactions at higher temperatures. However, the temperature demarcations are not sharp. For example, thermogenic methane can evolve at temperatures overlapping those attending microbial methanogenesis through low-temperature catagenesis, and the temperatures attending serpentinization that produces hydrogen, and ultimately methane, can occur at relatively low temperatures that also overlap the microbial range (Schrenk et al., 2013). While the relative abundances of $^{13}CH_3D$ in terrestrial settings was utilized as a tracer of the temperature of formation of methane, with equilibrium temperatures exhibited for thermogenic gases (Stolper et al., 2014; Young et al., 2017; Xie et al., 2021), it also became clear that departures from equilibrium were present (e.g., Wang et al., 2015; Stolper et al., 2015; Douglas et al., 2017; Young et al., 2017; Giunta et al., 2019). A focus on

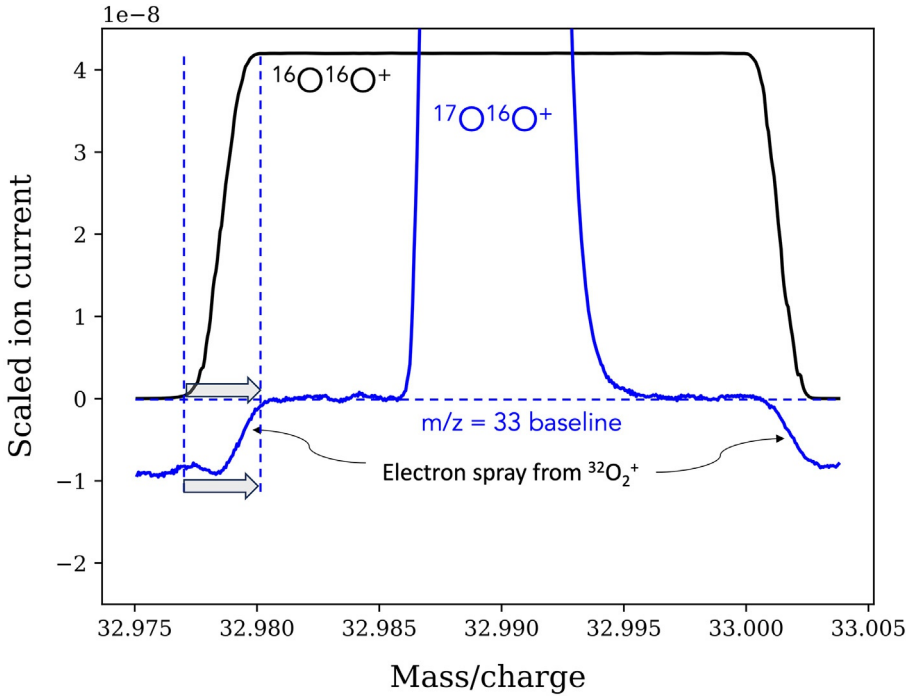

Fig. 8 O_2 peak shapes collected on the Panorama prototype HR-IRMS instrument illustrating lowering of the $^{17}O^{16}O^+$ baseline by secondary electrons produced by the $^{16}O^{16}O^+$ ion beam. Dashed horizontal line shows the $^{17}O^{16}O^+$ baseline when no beams are present. Vertical construction lines and block arrows illustrate the coincidence of the major ion beam hitting the edge of its entrance slit and the depression of the baseline for the $^{17}O^{16}O^+$ beam. Values for ion current (amps) are scaled for presentation: ion current for $^{16}O^{16}O^+$ is multiplied by 50×, and that for $^{17}O^{16}O^+$ by 1×10^6. The latter is also shifted by a factor of $+1.13 \times 10^{-7}$ after scaling to align the baselines. Accounting for these scalings, the actual shift in the $^{17}O^{16}O^+$ baseline due to secondary electrons is about 1×10^{-14} amps, or ∼ 10 mV with the 10^{12} Ω resistor of the amplifier used. Mass/charge refers to the mass-33 collector.

disequilibrium effects associated with microbialgenesis arose as these departures from equilibrium were found to be typical of microbial methane production in cultures and in non-marine natural environments, both through measurements (Douglas et al., 2016; Young et al., 2017; Gruen et al., 2018), and through modeling (Stolper et al., 2015; Wang et al., 2016; Young et al., 2017; Cao et al., 2019; Young, 2019). At the same time, microbial methanogenesis in some environments, particularly in marine sediments, appears to produce methane in near thermodynamic equilibrium at low temperatures (Ono et al., 2022; Liu et al., 2024). Departures from equilibrium are also evidenced during relatively low-temperature thermogenesis by cracking of hydrocarbons (Xie et al., 2021) and by oxidation of methane by atmosphere radicals OH^- and Cl^- (Whitehill et al., 2017; Haghnegahdar et al., 2017). The previously predicted effects of radicals on atmospheric methane isotopologue ratios have been confirmed through measurements of the relative concentrations of $^{13}CH_3D$ and $^{12}CH_2D_2$ in air (Haghnegahdar et al., 2023).

The combination of both $^{13}CH_3D$ and $^{12}CH_2D_2$ concentrations in a sample of methane has proven powerful in either establishing that thermodynamic equilibrium was attained for a sample of methane, or, conversely, for characterizing tell-tale departures from equilibrium caused by microbial activity in the form of microbialgenesis, aerobic oxidation of methane (AeOM), or anaerobic oxidation of methane (AOM) (Young et al., 2017; Young, 2019; Ash et al., 2019; Giunta et al., 2022; Liu et al., 2023). Thermodynamic equilibrium is demonstrated where departures from the stochastic distribution for the abundances of both $^{13}CH_3D$ and $^{12}CH_2D_2$, represented as $\Delta^{13}CH_3D$ and $\Delta^{12}CH_2D_2$ values, the per mil deviations in $^{13}CH_3D/^{12}CH_4$ and $^{12}CH_2D_2/^{12}CH_4$ from the stochastic ratios, respectively, are consistent with a single, concordant temperature.

Overcoming the challenges in measuring reliable $^{12}CH_2D_2/^{12}CH_4$ ratios (e.g., Fig. 7) has proven important in studies of the provenance of methane. The power of $\Delta^{12}CH_2D_2$ in characterizing reaction pathways during methane formation is a result of the combinatorial effect. This effect is a mathematical consequence of drawing from more than one isotopic pool for a given element when constructing a molecule (Yeung et al., 2015, 2016; Röckmann et al., 2016). In the case of methane, constructing a molecule from more than one pool of hydrogen with distinct D/H ratios can lead to negative $\Delta^{12}CH_2D_2$ values (Young et al., 2017). The effect has been demonstrated for methane in the laboratory (Taenzer et al., 2020). The sources of distinct D/H pools can be intracellular where each enzymatic step has a distinct D/H (Cao et al., 2019; Young, 2019) or from distinct exogenous sources, including H_2O and CH_3 (e.g., Taenzer et al., 2020). The combinatorial effect in this context can be explained in terms of how $\Delta^{12}CH_2D_2$ is calculated.

As an example, consider a sample of methane gas with $\delta D = -127.84$ ‰ relative to standard mean ocean water (V-SMOW) and $\delta^{13}C = -10.84$ ‰ relative to the Pee Dee Belemnite (V-PDB) standard, corresponding to a measured bulk D/H ratio of

1.3585×10^{-4} and a $^{13}C/^{12}C$ of 0.011115392. The measured $^{12}CH_2D_2/^{12}CH_4$ ratio in this example is 1.12012×10^{-7}. One computes the stochastic ratio from the measured bulk isotope ratios. Isotope-specific mole fractions for singly-substituted isotopologues are closely approximated as

$$\begin{aligned} x_D &= \frac{R_D}{1 + R_D} \\ x_H &= \frac{R_H}{1 + R_H} \\ x_{^{12}C} &= \frac{1}{1 + R_{^{13}C}}, \end{aligned} \tag{3}$$

where R_D is the bulk D/H ratio and $R_{^{13}C}$ is the bulk $^{13}C/^{12}C$ ratio. From the properties of probabilities, the stochastic isotope-specific mole fractions of $^{12}CH_2D_2$ and $^{12}CH_4$ where isotopes are distributed randomly across all isotopologues are

$$x_{^{12}CH_2D_2} = 6x_{^{12}C}x_D^2x_H^2 \tag{4}$$

and

$$x_{^{12}CH_4} = x_{^{12}C}x_H^4, \tag{5}$$

where the 6 in Eq. (4) refers to the 6 isotopic isomers for this species. In this example, the stochastic value for $x_{^{12}CH2D_2} = 1.09455 \times 10^{-7}$ and the stochastic value for $x_{^{12}CH4} = 0.9884696$. We therefore have for $\Delta^{12}CH_2D_2$

$$\Delta^{12}CH_2D_2 = 10^3\left(\frac{\left(^{12}CH_2D_2/^{12}CH_4\right)_{meas}}{\left(x_{^{12}CH_2D_2}/x_{^{12}CH_4}\right)_{stoch}} - 1\right) = -51.8, \tag{6}$$

where subscript "meas" refers to the measured isotopologue ratio and "stoch" refers to the stochastic ratio. Now we consider the possibility that these molecules were in fact constructed from two pools of hydrogen with distinct D/H ratios, with the average D/H being the measured bulk value in our methane. If α is the fractionation factor relating the D/H ratios for the two pools, we have

$$R_D = \frac{R_1 + \alpha R_1}{2}, \tag{7}$$

where R_1 is the D/H for one of the reservoirs, $\alpha R_1 = R_2$ is the D/H for the other reservoir, and R_D is the measured bulk ratio. Now the true stochastic ratio, given a priori knowledge of equal contributions from the two pools, is given by the corresponding mole fractions for the two pools, $x_{D(1)}$, $x_{D(2)}$ etc., so Eq. (4) becomes instead

$$x_{^{12}CH_2D_2} = 6x_{D(1)}x_{D(2)}x_{H(1)}x_{H(2)}x_{^{12}C}. \tag{8}$$

Similarly, the stochastic mole fraction for $^{12}CH_4$ is now

$$x_{^{12}CH_4} = x_{^{12}C}x_{H(1)}^2x_{H(2)}^2. \tag{9}$$

In our example, we choose an α value of 1.7, so the stochastic value for $x_{^{12}CH2D_2}$ is now 1.02098×10^{-7}, considerably less than the value obtained from the measured bulk D/H and $^{13}C/^{12}C$ ratios. The stochastic isotopic mole fraction for $^{12}CH_4$ is essentially the same, with $x_{^{12}CH4} = 0.9884696$. Applying Eq. (6) using the actual stochastic mole fraction from Eq. (8) one obtains $\Delta^{12}CH_2D_2 = 16.6$ ‰, or 68 per mil greater than the measured value.

The reason for the discrepancy is the mathematical truism that is apparent by simplifying the expressions for $\Delta^{12}CH_2D_2$. It is straightforward from Eqs. (3) through (7) that in the case of the average D/H,

$$\Delta^{12}CH_2D_2 = 10^3\left(\frac{\left(^{12}CH_2D_2/^{12}CH_4\right)_{meas}}{6R_D^2} - 1\right). \tag{10}$$

Eq. (10) shows that the value for $\Delta^{12}CH_2D_2$ is inversely proportional to the square of the arithmetic mean of the two D/H ratios for hydrogen pools 1 and 2. Conversely, when using the true D/H ratios comprising the molecules, we have

$$\Delta^{12}CH_2D_2 = 10^3\left(\frac{\left(^{12}CH_2D_2/^{12}CH_4\right)_{meas}}{6R_{D(1)}R_{D(2)}} - 1\right) \tag{11}$$

where now $\Delta^{12}CH_2D_2$ is inversely proportional to the square of the geometric mean of the two D/H ratios. The geometric mean will always be less than the arithmetic mean unless $R_{D(1)} = R_{D(2)}$ in our example, in which case they are equal. Thus in general, where molecular positions with distinct isotope ratios are indistinguishable, and the average isotope ratios rather than the site-specific isotope ratios are all that is accessible by the data (the usual case for IRMS), the calculated stochastic ratio of the multiply-substituted molecule to the major isotopologue will be overestimated. This in turn means Δ values derived from these overestimated stochastic ratios will be underestimated. This combinatorial effect is thought to be the dominant explanation for low $\Delta^{12}CH_2D_2$ values associated with microbial methanogenesis and other kinetic processes.

One important application of all of the newly acquired rare isotopologue data for methane is the distinguishing of microbialgenic gases from other sources. A valuable advantage of using $\Delta^{13}CH_3D$ and $\Delta^{12}CH_2D_2$ for this purpose is that these values are independent of carbon and hydrogen source isotope ratios (independent of substrate). One can use both bulk isotope ratios and clumped isotope data for a subset of methane analyses as the basis for a Bayesian statistical method to identifying methane produced by microbial methanogenesis. In this approach, the bulk isotope ratios are used as the prior probability for any given unknown datum in the Bayesian vernacular. A "Haldane" prior is used that is a beta function at each isotopic composition with both coefficients being 2 so that the value does not depend on the sample size. In this way finite priors in 2D space defined by $\delta^{13}C$ and δD values, have a maximum of 0.5. The map of mass-18 isotopologue compositions for the same data subset defines a likelihood function for any given unknown datum. In this case, Gaussian distributions at each pixel in 2D space, this time defined by $\Delta^{13}CH_3D$ and $\Delta^{12}CH_2D_2$ values, are assigned parameters that yield similar probabilities across the field spanned by the "training" data. An example for a contentious datum (Nothaft et al., 2021; Etiope, 2017) where $\delta^{13}C$ values are unusually high is shown in Fig. 9. This high $\delta^{13}C$ value of near 10 ‰ is unusual, and is either a substrate effect or an effect of oxidation of the methane gas. By combining the prior and likelihood values for this datum defined by measured $\delta^{13}C$, δD, $\Delta^{13}CH_3D$, and $\Delta^{12}CH_2D_2$ values, a posterior probability of 60% that this methane gas sample is microbial in origin is obtained, despite a prior probability of just 1% based on bulk isotope ratios alone (Fig. 9).

This is the first step toward the ultimate goal of developing reliable tracers for biogenicity given these methane isotopologue ratio measurements alone, as might be required, for example, by sampling on another Solar System body where geochemical constraints are minimal, and the isotopic compositions of sources are not constrained.

CH_3

A related application is isotope clumping in methyl groups, CH_3, derived from organic molecules (Lloyd et al., 2021). In this application, the CH_3 groups comprising CH_3-O-R are derivatized to form halogen species (CH_3I followed by conversion to the more volatile CH_3F and CH_3Cl species). Extraction of an intact moiety such as CH_3 from a condensed phase that preserves isotope clumping is reminiscent of the case for carbonates described above, in which CO_2 preserves the isotope clumping in the parent CO_3^{--}. The electron impact source cleaves the derivatized methyl groups from the halogen and measurements are made using the isotopic variants of CH_3^+. Precision is similar to that for methane. To date, measurements for CH_3 clumping have been made using a 253 Ultra HR-IRMS instrument. Here, the singly-substituted mass-16 isotopologues $^{13}CH_3^+$ and $^{12}CH_2D^+$, with an $m/\Delta m$ of ~5500, as well as an interfering mass-16 $^{12}CH_4^+$ adduct created in the electron impact source, are measured on distinct shoulders of a composite mass-16 peak ion peak with an instrumental MRP of 16,000. The multiply-substituted mass-17 isotopologues $^{13}CH_2D^+$ and $^{12}CHD_2^+$ define a similar $m/\Delta m$ of 5800. Methane isotopologues are produced in the source of the instrument in a manner analogous to the formation of CH_5^+ isotopic species when measuring methane. $^{13}CH_4^+$ formed in the source has an $m/\Delta m$ relative to $^{13}CH_2D^+$ of 11,000. While this overlap presents analytical challenges, these species have been resolved sufficiently with an instrumental MRP of 22,000 (Lloyd et al., 2021). The $m/\Delta m$ between $^{12}CHD_2^+$ and $^{13}CH_4^+$ is 12,400. With the MRP of 28,000 used in these measurements, the low abundance of $^{12}CHD_2^+$ requires a correction due to contributions from the tails of both $^{13}CH_4^+$ and $^{12}CH_3D^+$ on the low and high-mass sides of the analyte peak, respectively (relationships between the adduct interferences and the analyte are analogous to the situation for $^{12}CH_2D_2^+$ in methane shown in Fig. 7).

Lloyd et al. (2023) used these procedures to measure the relative concentration of $^{13}CH_2D$ in methoxyl groups (CH_3-O-R) in wood lignin, seeking a proxy for the rate of photorespiration relative to carboxylation. Both processes are catalyzed by the enzyme

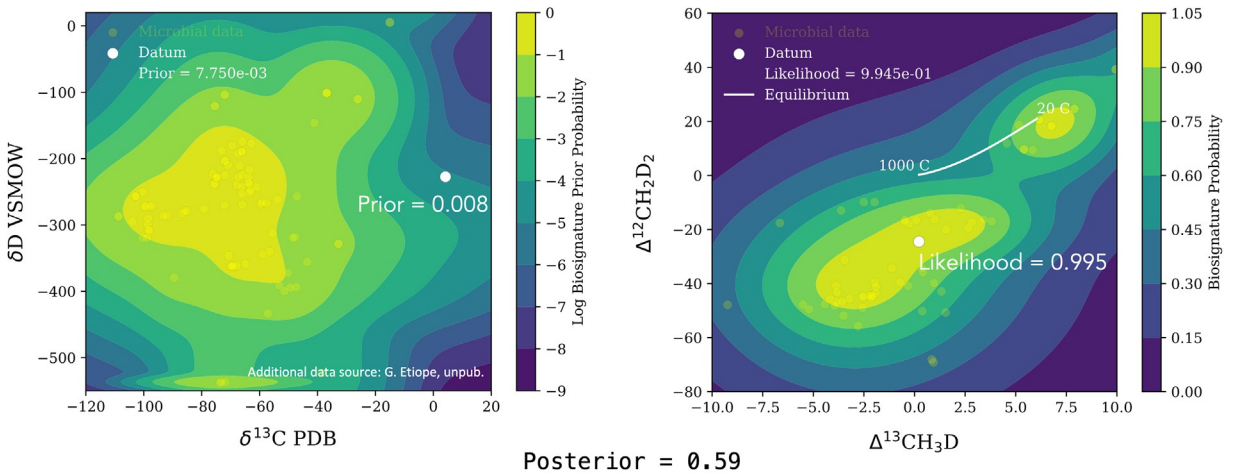

Fig. 9 Prior probability contours (left) and likelihood contours (right) for a set of methane training data, compared with a single datum from the Oman ophiolite (Nothaft et al., 2021). The prior probability based on bulk isotope ratios, affected by substrate isotope ratios, and the likelihood function based on $\Delta^{13}CH_3D$ and $\Delta^{12}CH_2D_2$ values, combine to yield a posterior probability that the datum shown is microbial in origin. The curve in $\Delta^{13}CH_3D$ vs. $\Delta^{12}CH_2D_2$ space represents values at thermodynamic equilibrium for the specified temperatures, for reference.

ribulose-1,5-bisphosphate carboxylase/oxygenase (RuBisCO) that is responsible for CO_2 fixation by photosynthesis, with the former resulting in liberation of initially fixed CO_2 and the latter consuming CO_2. Due to their opposing effects on the fate of CO_2, the ratio of the rate of photorespiration to the rate of carboxylation is a factor influencing the total production of organic matter by photosynthesis (gross primary production, GPP). $\Delta^{13}CH_2D$ values derived from wood lignin depart from the equilibrium curve in a plot of $\Delta^{12}CHD_2$ vs $\Delta^{13}CH_2D$. The methyl groups exhibit markedly negative $\Delta^{12}CHD_2$ values that apparently arise from combinatorial effects like those seen for methane $^{12}CH_2D_2$, and the $\Delta^{13}CH_2D$ values are significantly greater than expected for ambient temperatures (Lloyd et al., 2021). However, systematic kinetic effects related to reaction pathways have been identified. Lloyd et al. (2023) found that $\Delta^{13}CH_2D$ decreases with an increase in the rate of photorespiration relative to carboxylation. A doubling of the ratio of photorespiration to carboxylation from about 0.25 to 0.5 is associated with a decrease in $\Delta^{13}CH_2D$ of about 1.4‰. With this tool it should be possible to track rates of photorespiration relative to carboxylation using lignin on both modern and ancient wood samples. Lloyd et al. (2023) point out that methoxyl D/H can also be used as a tracer of this rate ratio, but it requires normalizing to the D/H of the substrate (i.e., local source) water. As in other applications of multiply-substituted isotopologues, the use of clumping in a single molecular species (CH_3) permits estimating these relative rates even in ancient samples where the isotopic composition of the substrate water is not known. Results of sampling of trees from around the globe indicates that variability in wood $\Delta^{13}CH_2D$ values vary with the photorespiration/carboxylation rate ratio that is in turn controlled by a combination of growing season temperature and water availability. $\Delta^{13}CH_2D$ values from wood lignin comprise a useful tool for disentangling the effects of changing climate on GPP and associated climatic feedbacks related to rising atmospheric CO_2 concentrations.

N_2

Nitrogen comprises most of Earth's atmosphere and is crucial to the biosphere. It moves between the atmosphere and biosphere by a cycle involving microbial fixation of nitrogen to produce NH_4^+ that is oxidized by microbial chemolithotrophic oxidation (nitrification), and reduction of oxidized N by microbial anaerobic respiration (denitrification). Nitrogen is also transferred between surface environments and the deep Earth by subduction of sediments and release of dissolved gases during volcanic eruptions. It is thus in some ways analogous to noble gases in comprising a tracer of exchange between the surface and deep mantle. Because it consists of just two isotopes, ^{15}N and ^{14}N, the bulk isotopic composition of nitrogen, $^{15}N/^{14}N$, while useful, is also limited as a tracer. Analyses of doubly-substituted isotopologues of N_2 is a new geochemical tool made possible by high-mass-resolution mass spectrometry. The key discovery is that atmospheric N_2 has a substantial $^{15}N^{15}N$ disequilibrium enrichment of 19‰ (Yeung et al., 2017) and that this may be used to unambiguously quantify air contributions in natural samples where the origin of dinitrogen is not clear.

High-mass-resolution mass spectrometry is necessary for the separation of $^{15}N^{15}N^+$ from ubiquitous backgrounds of nitrogen monoxide $^{14}N^{16}O^+$. Because it is present as a background in the instruments, offline purification is not a solution. The $m/\Delta m$ between ^{30}NO ($^{14}N^{16}O^+$) and $^{30}N_2$ ($^{15}N^{15}N^+$) is 13,400, requiring an instrumental mass resolving power of as much as ~65,000 using the zero-order estimate that instrumental MRP needs to be approximately 5× the $m/\Delta m$ for effectively baseline separation of two species. In practice, an MRP of ~4 times the $m/\Delta m$ is sufficient for useful accuracy and precision at tenths of per mil (e.g., Fig. 10). At the time of this writing, $^{15}N^{15}N$ measurements have been done on the prototype Nu Instruments Panorama HR-IRMS at typical mass resolving powers of about 60,000 and with narrow collector slits.

Accurate measurements also require resolving the abundances of $^{14}N^{14}N^+$, $^{14}N^{15}N^+$ and $^{15}N^{15}N^+$ ions from ionized isotopologues of carbon and nitrogen monoxide. Specifically, ^{28}CO ($^{12}C^{16}O^+$) and $^{29}CO^+$ ($^{13}C^{16}O^+$ and $^{12}C^{17}O^+$) are interferences for $^{28}N_2$ ($^{14}N^{14}N^+$) and $^{29}N_2$ ($^{14}N^{15}N^+$). The $m/\Delta m$ separating $^{12}C^{16}O^+$ from $^{14}N^{14}N^+$ is 2500, while values of 6000 and 7000 separate $^{13}C^{16}O^+$ and $^{12}C^{17}O^+$ from $^{14}N^{15}N^+$, respectively. Based on the general relationship between mass resolving power to inter-species $m/\Delta m$ (Fig. 6), mass resolving powers of at least 12,500, 30,000 and 35,000, respectively, are required to separate N_2 from CO interferences for integer masses 28 and 29. These values are achievable with the new HR-IRMS instruments, while classical gas-source IRMS instruments, for which mass resolving powers are <1000, would require quantitative removal of CO from N_2 samples during the preparation of samples. The most pernicious mass interference in this application is that between $^{12}C^{18}O^+$ and $^{15}N^{15}N^+$, however. The $m/\Delta m$ separating these ions is 28,275, requiring an MRP of order 150,000 for clean separation (Fig. 10). Fortunately, a concentration of about 2 ppm or more of $^{12}C^{18}O$ is required to substantively affect results; natural abundances of $^{12}C^{18}O$ are usually sufficiently low that the effects of any trace carbon in a sample of N_2 is less than analytical uncertainties of tenths of per mil.

Measurements are reported as $\delta^{29}N_2$ and $\delta^{30}N_2$ (Fig. 11) values, the per mil deviations in $^{29}N_2/^{28}N_2$ and $^{30}N_2/^{28}N_2$ ratios from those in air, where $\delta^{29}N_2 = 1000 \times (^{29}R_{sample}/^{29}R_{air} - 1)$ (‰) and $^{29}R = (^{14}N^{15}N + {}^{15}N^{14}N)/^{14}N^{14}N$ for the gas of interest. Since $(^{14}N^{15}N + {}^{15}N^{14}N)/^{14}N^{14}N$ equals $2 \times (^{15}N/^{14}N)$ for both the sample and the standard, $\delta^{29}N_2$ is equivalent to the bulk isotope ratio expressed as $\delta^{15}N = 1000 \times (^{15}R_{sample}/^{15}R_{air}\text{-}1)$ where $^{15}R = {}^{15}N/^{14}N$. For $^{30}N_2/^{28}N_2$, $\delta^{30}N_2 = 1000 \times (^{30}R_{sample}/^{30}R_{air} - 1)$ (‰) where $^{30}R = {}^{15}N^{15}N/^{14}N^{14}N$ for the gas of interest. The Δ_{30} is a tracer that is the measure of departures from a purely stochastic distribution of ^{15}N and ^{14}N atoms comprising the isotopic molecular species. It is defined such that $\Delta_{30} = 1000 \times (^{30}R/(^{15}R)^2\text{–}1)$ (‰). The value $(^{15}R)^2$ represents the stochastic relative abundance of $^{30}N_2$, and reflects the fact that the probability of forming $^{30}N_2$ from a purely random distribution of ^{14}N and ^{15}N atoms across all nitrogen isotopologues is the square of the probability of finding molecules with just one ^{15}N. In practice, Δ_{30} is the vertical deviation from the lower mass-dependent curve in Fig. 11. In reality, the formation of $^{15}N^{15}N$ is not purely random. The relatively low vibrational energy of this doubly-substituted molecule

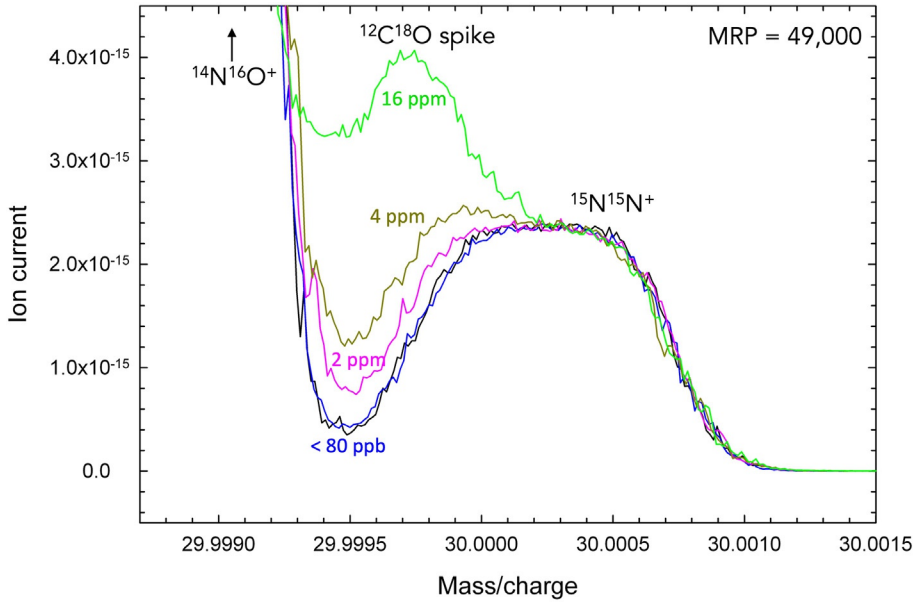

Fig. 10 Peak shapes for $^{15}N^{15}N^+$, background $^{14}N^{16}O^+$, and several concentrations of $^{12}C^{18}O^+$ spike at integer mass/charge of 30 obtained on the Panorama HR-IRMS prototype at an MRP of 49,000. $^{14}N^{16}O^+$ is separated from $^{15}N^{15}N^+$ while $^{12}C^{18}O^+$ is only partially separated from $^{15}N^{15}N^+$. Ion currents calculated from counts per second measured using a secondary electron multiplier. This plot shows data first presented by Yeung et al. (2017).

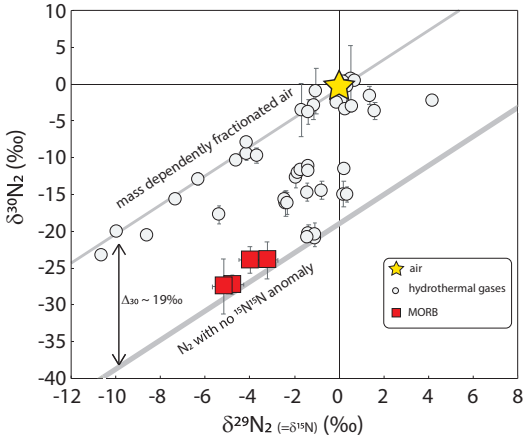

Fig. 11 Isotopic composition of N_2 from natural samples for $\delta^{29}N_2$ and $\delta^{30}N_2O$. Mass-dependent fractionation curves for air and high-temperature stochastic N_2 are shown. Air data are from Yeung et al. (2017). Mid-ocean ridge basalts and most hydrothermal samples are from Labidi et al. (2020, 2021). See Yeung et al. (2017) for details in the establishment of the mass-dependant line with no $^{15}N^{15}N$ excess. Figure modified from Labidi J and Young E (2022) The origin and dynamics of nitrogen in the earth's mantle constrained by 15N15N in hydrothermal gases. *Chemical Geology* 591: 120709.

results in a thermodynamic driving force for its formation, which is accentuated at the lower temperatures. At geochemically relevant temperatures ranging from 200 to 1000 °C, equilibrium among N_2 isotopologues results in Δ_{30} values from 0.5 to 0.1‰, respectively (Yeung et al., 2017).

The first discovery using the ability to measure the N_2 mass-30 clumped isotopologue has been that all air samples, from various altitudes and from air dissolved in shallow oceanic waters, all have the same elevated Δ_{30} relative to the stochastic distribution (Yeung et al., 2017). Average Δ_{30} of air is 19.1 ± 0.3 ‰ (Yeung et al., 2017). Considering analytical uncertainties of about 0.1‰ for individual measurements, the $^{15}N^{15}N$ excess measured in air is a large disequilibrium signal that provides considerable purchase on tracing air. Electrolysis experiments can be used to generate variable Δ_{30} values, and by analogy with photochemistry involving nitrogen and oxygen, the $^{15}N^{15}N$ excess observed in air has been attributed to N_2 photochemistry in the upper atmosphere (Yeung et al., 2017).

The potential to use Δ_{30} as a tracer of air in nature where other tracers deliver ambiguous estimates was recognized immediately (Yeung et al., 2017). This is because N_2 molecules synthesized from a range of geological and biological processes have Δ_{30} values of 0.0 ± 0.5 ‰. This is true of high-temperature N_2, as prescribed by thermodynamic equilibrium, but notably also of N_2 synthesized

by microbial life (Yeung et al., 2017). Using that important constraint, Yeung et al. (2019) quantified the amount of biological N_2 mixed with air-derived N_2 in a series of agricultural soils, demonstrating that the Δ_{30} tracer may be useful in constraining productivity in natural environments.

Labidi et al. (2020, 2021) used the $^{15}N^{15}N$ tracer to determine the amounts of air-derived N_2 from volcanic N_2 in hydrothermal gases from plumes and arcs. The work relies on the observation that high-temperature N_2 degassed from silicate melts at crustal depths has a characteristic Δ_{30} of 0 ‰. This is demonstrated by the measurements of the nitrogen isotopologue compositions of mid-ocean ridge basalts (Labidi et al., 2020) (Fig. 11). When the volcanic nitrogen reaches the surface, it may acquire elevated Δ_{30} values by mixing with air-derived gases in the hydrothermal systems. Using Δ_{30} as a tracer in hydrothermal systems is possible to the extent that atmospheric signatures are not reordered when atmospheric fluids undergo heating in the sub-surface. Resistance to reordering is indicated by experimental and natural data obtained thus far (Labidi and Young, 2022). Nonetheless, the characteristic timescales necessary to effectively reset an elevated Δ_{30} value among N_2 molecules as a function of temperature could extend to geological timescales, and more experimental work permitting extrapolation of the kinetics to these longer times is warranted.

The work on hydrothermal systems demonstrates that atmospheric nitrogen is ubiquitous in hydrothermal samples, even in samples with venting temperatures up to 400 °C, where no atmospheric O_2 is detected, and where noble gas relative abundances would predict limited atmospheric contributions (Labidi et al., 2020, 2021). Perhaps most importantly, air-derived N_2 is recognized unambiguously on the basis of atmospheric Δ_{30} values, but this same N_2 gas may possess definitively non-atmospheric $^{15}N/^{14}N$. This is illustrated on Fig. 11, where samples distributed to markedly low $\delta^{15}N$ values on the air fractionation line. The low $\delta^{15}N$ of air-derived samples must reflect mass-dependant fractionation of the N_2 isotopologues in the sub-surface. Gas-water kinetic isotope exchanges have so far been favored as a mechanism to account for the negative $\delta^{15}N$ values associated with atmospheric Δ_{30} (Labidi and Young, 2022). As an example, one can compare basalt samples shown in Fig. 11 that have low $^{15}N/^{14}N$ and a low Δ_{30} values with hydrothermal samples with similarly low $^{15}N/^{14}N$ but elevated Δ_{30}. The $\delta^{15}N$ values of the hydrothermal samples are negative, resembling values observed in mid-ocean ridge basalts, but their Δ_{30} requires they are fully air derived. This means that without Δ_{30} measurements, many hydrothermal samples with low $\delta^{15}N$ are easily confused with mantle-derived gases.

Other findings have been leveraged using the $^{15}N^{15}N$ tracer, including an objective method to determine the true $\delta^{15}N$ of the volcanic endmembers in hydrothermal samples (Labidi et al., 2020). This is based on simple extrapolation of multi-component mixing relationships to endmembers with $\Delta_{30} = 0$ ‰. The potential to extrapolate any trends to a known high-temperature, air-free endpoints where Δ_{30} is 0 ‰, as prescribed by thermodynamics, allows one to disambiguate the high-temperature components that are intermingled with variable amounts of fractionated air in hydrothermal systems. Doing so exposes the true geochemical features of the purely volcanic components, and provides unique constraints on the deep cycle of nitrogen.

O_2

Measurements of the doubly-substituted isotopologues of dioxygen, $^{18}O^{18}O$ and $^{18}O^{17}O$, provide an example of a new geochemical proxy made practical by improvements in IRMS technologies. Measurements of mass-36 and mass-35 O_2 were first made on a low-mass-resolution, classical IRMS instrument (Yeung et al., 2012). The primary difficulty with this method is separating $^{36}Ar^+$ from $^{18}O^{18}O^+$. The $m/\Delta m$ for $^{36}Ar^+$ vs. $^{18}O^{18}O^+$ is 1170, suggesting that resolving this interference would ideally involve an MRP of about 5000. Since this is significantly beyond the capability of low-mass-resolution IRMS instruments, offline purification is required when these instruments are used. However, even with >99% efficiency of O_2-Ar separation, a significant interference from trace ^{36}Ar can persist. Also, the hydride interference for mass-36 O_2, $H^{35}Cl$, has a $m/\Delta m$ of 1663, suggesting an MRP of 8000 would be required for clean separation. What is more, $^{12}C_3$ is a background mass interference with an $m/\Delta m$ for $^{18}O^{18}O$ of 21,428, suggesting a bare minimum MRP value of perhaps 60,000 is needed to partially resolve these species, and an MRP of ~100,000 is required to completely resolve them. Measurements of $^{18}O^{17}O$ are equally challenging because of the rarity of this molecule. These numerous interferences severely hinder accurate O_2 clumping measurements on low-mass-resolution instruments.

In the first paper reporting the successful analysis of $^{18}O^{18}O$ and $^{18}O^{17}O$ in air by Yeung et al. (2012), sub-ambient-temperature gas chromatography was used to purify O_2. This work demonstrated that tropospheric O_2 is continuously exchanging isotopes with ground-state atomic oxygen, $O(^3P)$, resulting in abundances of $^{18}O^{18}O$ and $^{18}O^{17}O$ approaching ambient temperatures at different levels in the atmosphere. In a followup using the same low-resolution mass spectrometry method, Yeung et al. (2014) showed that Δ_{36} and Δ_{35} values (per mil deviations in $^{18}O^{18}O$ and $^{18}O^{17}O$ from the stochastic distribution) in the troposphere are the result the competition between the rate of $O(^3P) + O_2$ isotope exchange, leading to thermodynamic equilibrium among O_2 isotopologues at tropospheric temperatures (e.g., $\Delta_{36} \sim 2$‰), and vertical transport from the stratosphere where O_2 equilibrated at lower temperatures (with $\Delta_{36} \sim 2.5$‰) is delivered from the stratosphere to the troposphere. The prediction was made that biological processes may well have identifiable non-equilibrium Δ_{36} and Δ_{35} signatures. This prediction of a biological signature was verified shorty after (Yeung et al., 2015). The "anti-clumping" bias against heavy isotope pairing in photosynthetic O_2 was explained as a consequence of what was later referred to as the combinatorial effect (see above).

This early work showed that because Δ_{36} (and Δ_{35}) values in the troposphere depend on the concentration of $O(^3P)$, it could prove to be a proxy for ozone concentrations in the troposphere over time. This provided incentives to improve the precision of Δ_{36} and Δ_{35} measurements. Improvements in precision were achieved initially using a medium-resolution single-focusing IRMS with a maximum MRP of ~4000 (Nu Instruments modified Perspective SI), leading to an improvement in Δ_{36} precision by a factor of ~5×. The HR-IRMS instruments (253 Ultra, Panorama) make measurements of Δ_{36} straightforward (e.g. Laskar et al., 2019).

Enhancements in precision afforded by improved mass resolution brought the development of Δ_{36} as a proxy for troposphere chemistry over time. About 3/4 of the rare isotopologue concentration in tropospheric O_2 arises from isotope exchange with $O(^3P)$ with the rest coming from the stratosphere. As is the usual case, isotope clumping is enhanced at lower temperatures at equilibrium. Therefore, an increase in the exchange between $O(^3P) + O_2$ due to increases in $O(^3P)$, and thus O^3, causes a decrease in tropospheric Δ_{36} values due to a closer approach to the higher temperatures at ground level as compared to the stratosphere (Yeung et al., 2021). Yeung et al. (2019) made use of this relationship by measuring the $^{18}O^{18}O$ concentrations in air trapped in polar firn and ice as a monitor of O^3 concentrations from the turn of the 17th century to today, thus documenting the anthropogenic increase in this important molecule during the 20th century.

H_2

The equilibrium distribution of protium (^1H or H) and deuterium (^2H or D) atoms in dihydrogen molecules was investigated by Rittenberg et al. (1934). Indeed, the equilibrium: $^1H_2 + D_2 = 2\ ^1HD$ is in some ways the archetypical example of a reaction leading to a "clumped" isotopologue (e.g., Richet et al., 1977). Since then, owing to the large fractional difference in mass between H (^1H) and D (^2H), doubly-deuterated dihydrogen has been used as tracer of reaction pathways and reaction rates. Deuterium clumping in dihydrogen molecules at natural abundances and in geochemically-relevant environments is only now becoming practical as a tool with the advent of HR-IRMS instruments.

Popa et al. (2019) developed methods for measuring the relative concentrations of DD in dihydrogen using the 253 Ultra HR-IRMS. The primary difficulty is separating the DD^+ beam that has a low abundance of 2×10^{-6} relative to total hydrogen from $^1H_2D^+$ that forms in the electron impact source. The $m/\Delta m$ for these species is 2600, and Popa et al. (2019) used an MRP of about 18,000 to 20,000 to obtain separation for analysis of $DD/^1H^1H$. They used a relatively wide collector slit so the DD^+ ion beam is measured on the low-mass shoulder of the $^1H_2D^+$ interference using an ion counter. They showed that their results were consistent with the expected variations in ΔDD, the per mil departure from the stochastic distribution of ^1H and ^2H, with temperature in the laboratory.

Mangenot et al. (2023) used a similar method to examine the effects of hydrogenotrophic microbial production of methane on the ΔDD values of the source hydrogen gas. Their results indicate that during methanogenesis, the source H_2 is progressively mixed with H_2 equilibrated with respect to the reaction $^1H_2 + D_2 = 2\ ^1HD$ at the ambient temperature of the reaction (i.e., equilibrium ΔDD values are attained). This mixing phase ultimately gives way to nearly complete re-equilibration of the H^2 gas, requiring significant back reaction involving hydrogen from water at thermodynamic equilibrium and a significant return flux of equilibrated dihydrogen from the cells to the headspace gas. The equilibration is rapid even where the methanogenesis is vigorous and kinetic isotope partitioning should be favored. The conclusion is that hydrogenotrophic microbial methanogenesis should drive H_2 to equilibrium ΔDD values at ambient temperatures in natural settings.

Mangenot et al. (2023) also obtained ΔDD values for H^2 from the Rainbow, Ashadze, and Lost City deep-sea hydrothermal vent systems that indicate equilibration with their host vent fluids. In the case of Lost City, low temperatures of about 20 to 80 °C derived from ΔDD values match the temperatures of the venting fluids of 20 to 100 °C. The hydrogen gas from the Rainbow and Ashadze vents have ΔDD values consitent with equilibration at the ~350 °C temperatures of the vent fluids there. These results indicate that the DD isotopologues of H_2 are in thermo dynamic equilibrium with the host vent fluids in these hydrothermal systems. This is true even where D/H equilibrium between H_2 and H_2O is not indicated. Interestingly, Labidi et al. (2020) found that $\Delta^{12}CH_2D_2$ in methane at the Von Damm, Lucky Strike, Rainbow, and Lost City deep-sea hydrothermal systems also record the vent fluid temperatures, suggesting that the relative concentrations of DD and $^{12}CH_2D_2$ both equilibrated with their host vent fluids. Values for $\Delta^{13}CH_3D$ are not equilibrated at the lower vent fluid temperatures at Lost City, however. Since both hydrogen and methane at Lost City almost certainly formed at higher temperatures than the venting fluid (e.g., Wang et al., 2018; Labidi et al., 2020), post-formation equilibration of doubly-deuterated isotopologues of hydrogen and methane seems to be especially rapid even at relatively low temperatures of less than ~100 °C.

N_2O

The trace concentration of nitrous oxide, N_2O, in the atmosphere belies its importance. It is a greenhouse gas and contributes indirectly to destruction of ozone in the upper atmosphere (Ostrom and Ostrom, 2017). The atmospheric budget of N_2O is the result of a myriad of sources and sinks. Sources include microbial denitrification and nitrification on land, in lakes, and in the oceans, as well as anthropogenic sources, including agriculture. Major sinks include photolysis in the upper atmosphere by reaction with the excited state of atomic oxygen, $O(^1D)$, liberated by the photodissociation of ozone (Ostrom and Ostrom, 2017). Understanding the contributions of various sources and sinks to the N_2O budget is an important facet of understanding climate change.

The isotopomers of N_2O constitute a wealth of information regarding formation pathways for nitrous oxide because the molecules are composed of two elements with multiple isotopes, and the molecules are asymmetrical. This combination results in 12 isotopic isomers (isotopomers). Excluding the species with relative abundances of $\leq 2 \times 10^{-6}$ (e.g., those with ^{17}O or triply-substituted), the relevant isotopomers are reduced from 12 to 7, including $^{14}N^{14}N^{16}O$ (integer molecular mass 44), $^{14}N^{15}N^{16}O$ and $^{15}N^{14}N^{16}O$ (mass 45), $^{15}N^{15}N^{16}O$ and $^{14}N^{14}N^{18}O$ (mass 46), and $^{14}N^{15}N^{18}O$ and $^{15}N^{14}N^{18}O$ (mass 47).

There is a rich history of measuring the position-specific nitrogen isotopic compositions of N_2O in which the central nitrogen, labelled α, and the terminal nitrogen, labelled β (as in $N_2O = N^{\beta}N^{\alpha}O$), can be distinguished by distinct $^{15}N/^{14}N$ ratios. The nitrogen isotopic compositions can be obtained using IRMS because N_2O^+ ions are cleaved in the electron impact source to produce NO^+

ions that are about 1/3 the abundance of N_2O^+ ions (Toyoda and Yoshida, 1999; Brenninkmeijer and Röckmann, 1999). The NO^+ fragments produced in the source are composed of the central (α) nitrogen atoms still bonded to oxygen ($N^{\alpha}O^+$). The ratio of $^{15}N^{16}O^+/^{14}N^{16}O^+$ at mass/charge values of 31 and 30 thus provides a measure of the isotopic composition of the α site. Due to interferences (e.g., the $m/\Delta m$ between $^{15}N^+$ and doubly-ionized $^{14}N^{16}O^{++}$ in the source is 13,400), an interference-free measurement of the ion beam ratio $^{15}N^+/^{14}N^+$ cannot be obtained to measure the isotopic composition of the terminal β fragment. Rather, the latter must be calculated from mass balance between the α site ratio and the bulk $^{15}N/^{14}N$ ratio obtained from the bulk N isotope ratios, measured as ($^{14}N^{15}N^{16}O^+$ + $^{15}N^{14}N^{16}O^+$) /$^{14}N^{14}N^{16}O^+$ ratios.

The site preferences for ^{15}N in N_2O, often referred to as $SP = \delta^{15}N^{\alpha} - \delta^{15}N^{\beta}$, has proven useful as a tracer of the microbial origins of these molecules (e.g., Yoshida and Toyoda, 2000; Toyoda et al., 2017). Like clumped isotope concentrations, and unlike bulk N isotope ratios, SP is not influenced by variable substrate $^{15}N/^{14}N$ ratios. Denitrifying microbes that reduce nitrate, NO_3^-, as well as nitrifying microbes that reduce nitrite, NO_2^-, produce N_2O with SP values of about 0‰, meaning that ^{15}N shows no clear preference for either the terminal or central N positions. Conversely, N_2O produced by oxidation by nitrifying microbes (e.g., oxidation of NH_4^+) exhibits significant enrichment in ^{15}N in the central N position, with SP values of about 30‰ (Sutka et al., 2006). This enrichment is in qualitative agreement with expectations from equilibrium thermodynamics that ^{15}N should strongly favor the central α position over the β position by nearly 50‰ at 300 K (Wang et al., 2004). Oxidation pathways (nitrification), therefore, produce a strong SP signal in the product N_2O in response to thermodynamic driving forces while reduction (denitrification) pathways produce no clear site-specific preference for ^{15}N. Denitrification and nitrifier denitrification are not distinguished by the site preference.

Studies of the complex isotopomer system comprising N_2O is a clear target for HR-IRMS technology. Magyar et al. (2016) used a 253 Ultra HR-IRMS to investigate the clumping of N and O isotopes in N_2O. In this work, the isotopic variants of N_2O^+ and NO^+ fragments were measured with an instrumental MRP of about 18,000. This MRP is sufficient to produce resolved peak flats on composite peaks for many of the analytes. Among the interferences are $^{16}O^{17}O^+$ overlapping $^{15}N^{18}O^+$, with an $m/\Delta m$ of about 6300 at integer mass 33, $^{14}N^{14}N^{17}O^+$ impinging on the $^{14}N^{15}N^{16}O^+$ and $^{15}N^{14}N^{16}O^+$ isomers at mass 45 with an $m/\Delta m$ of 6300, and $^{15}N^{15}N^{16}O^+$ on $^{14}N^{14}N^{18}O^+$ with an $m/\Delta m$ of 4500 at mass 46. In addition, extraneous background species like CO_2 produce additional interferences. One is $^{13}C^{16}O^{18}O^+$ overlapping the clumped isomers $^{14}N^{15}N^{18}O^+$ and $^{15}N^{14}N^{18}O^+$ at mass 47, with an $m/\Delta m$ of 9570, which presents a significant challenge with an instrumental MRP of 18,000 that is only twice the minimum resolution. Other interferences that cannot be resolved at all, including mass-45 CO_2 from mass-45 N_2O, are accounted for using background subtractions (Magyar et al., 2016). As in prior studies, a correction to the site-specific N isotope ratios of about 10‰ is necessitated by scrambling of the site-specific isotope ratios in the electron impact source.

As described above, earlier work leads to the expectation that denitrifying bacteria will produce N_2O with no pronounced site preference for ^{15}N. The HR-IRMS results for N_2O produced by denitrifying bacteria are generally consistent with this result, with an average value for SP of -3.7 ± 0.3‰ (Magyar et al., 2016). This study further shows that the clumped equivalent, i.e., site preference for ^{15}N among the $^{14}N^{15}N^{18}O$ and $^{15}N^{14}N^{18}O$ mass-47 isomers, is similar to the singly-substituted value, with an α site preference of -0.5 ± 3.8‰ relative to the β position. These values, that are either negative (for the $N_2^{16}O$ isotopologues) or indistinguishable from zero (for the $N_2^{18}O$ isotopologues), differ from the values predicted on the basis of thermodynamic equilibrium (Wang et al., 2004; Magyar et al., 2016). The ^{15}N isotope is thermodynamically favored to occupy the central (α) position in N_2 by tens of per mil at room temperature, and so the denitrification SP effects are clearly kinetic. Conversely, the mass-47 clumping (sum of both mass-47 isomers, $^{14}N^{15}N^{18}O$ and $^{15}N^{14}N^{18}O$, relative to the stochastic distribution) produced by these denitrifying bacteria, which we can refer to as Δ_{47} for N_2O (Wang et al., 2004), was found to be 0.4 ± 0.4‰, a close match to expectations for thermodynamic equilibrium at the room temperature of the culture experiments. These results provide a window into the mechanism of N_2O assembly during denitrification. One interpretation is that N-O bonds in the N_2O precursors respond to equilibrium thermodynamic driving forces, resulting in equilibrium clumped isotope distributions, while N-N bonds, representing final assembly of N_2O, are kinetic in origin (Magyar et al., 2016).

Orbitrap Fourier-transform IRMS

Science motivation

Utilization of HR-IRMS instrumentation has yielded a wealth of new information over the last decade. Despite the significant technological advances, including use of electrostatic sectors, large-radii mass analyzers, and improved collector sets (e.g., ion counters, narrow collector slits), there is the need for even greater mass resolution and sensitivity. Intramolecular isotopic distributions are not generally determined by IRMS except for the simplest molecules where fragmentation in the electron impact source can be used to calculate position-specific isotope ratios, as in the case of N_2O (see above), and only then with great difficulty (see the review by Ostrom and Ostrom, 2017). This fundamental limitation of requiring measurements to be done on simple gases has restricted the ability to interrogate intra-molecular isotopic distributions for more massive organic analytes, for example. Where simple gases are produced from larger molecules, as in the case of compound-specific carbon isotopic analysis of organics by carrier-flow IRMS, position specificity is lost. Where higher molecular weight volatiles are introduced directly into magnetic sector mass spectrometers, fragmentation and adduct formation results in isobaric interferences that cannot be resolved with HR-IRMS instruments.

There is a requirement, therefore, for instruments that can measure isotopologue ratios of intact molecular ions or fragment ions at extremely high mass resolution (ca. MR = 500,000). An instrument with these capabilities theoretically provides access to all or most of the isotopically substituted forms of the molecular ion, providing the user with information on the distribution of the isotopic substitutions rather than just the molecular average. These additional isotopic dimensions and the ability to simultaneously measure the isotopologue ratios for multiple elements in individual molecules substantially increases the isotopic information from a single analysis.

Successful experiments have been performed on multiple types of instruments with these goals in mind. Nuclear Magnetic Resonance (NMR), Time-of-flight mass spectrometry (TOF MS) and Fourier-transform ion cyclotron mass spectrometry (FTICR) all have the analytical capability to measure molecular ions and achieve high mass resolutions. The type of instrument that has recently proven most successful when applied to natural-abundance isotopologue ratio measurements of intact molecular ions is the Thermo Scientific Hybrid Orbitrap™ MS instrument family. While originally conceived as a means of measuring relative concentrations of molecules with high mass resolution, this technology is being harnessed for quantitative measurements of isotopologue ratios with numerous geochemical applications (Eiler, 2007). These are MS/MS systems with a quadrupole MS for m/z transmission range determination followed by a C-trap + Orbitrap analyzer (Makarov et al., 2006). The success of this type of instrument can be attributed to the low cost, compact size, and routine coupling with GC and LC sample introduction systems.

Principles of hybrid Orbitrap mass analysis

The Orbital ion trap analyzer originated with the Kingdon trap (Kingdon, 1923) and is based on the principle of a central and outer electrode between which a voltage potential is applied. When ions are injected into the cylindrical trap volume they are attracted to the central electrode, and, given sufficient inertia and angular momentum, they enter into orbital paths around the central electrode (Fig. 12). Early versions with static, homogeneous electrical potential fields showed poor mass resolution due to the main controls on orbital path being ion velocity and radius. Makarov (2000) introduced an orbital ion trap with electrode geometries resulting in a curved potential field that adds an axial component to the introduced ion's orbital path.

This approach was different from previous orbital ion trap analyzers in that the m/z of a given ion is determined by the frequency of harmonic oscillations along the trap axis and not from differences in radial frequency mode (the latter being how orbital ion trapping is used in FTICR where containment is by a large magnetic field). This new approach of deriving m/z modes from axial harmonic oscillations in a curved electrical potential field was coined the "Orbitrap" analyzer.

Another significant technological improvement was first outlined by Makarov et al. (2006), wherein a new type of curved, radio frequency-only quadrupole, the "C-trap" was implemented as a way of storing ions and homogenizing their energy distribution prior to injection into the Orbitrap analyzer. While this development was initially introduced to deal with challenges related to increasing the ion injection capacity and removing variations in kinetic ion energies for high-mass range un-targeted molecular analysis, it is critical for IRMS applications. Only by having the ability to store and collisionally cool ions is the instrument able to introduce ion packets to the Orbitrap analyzer with stable mass discrimination and repeatable resolution and mass accuracy.

Despite the technical advantages that this type of instrument possesses, there are also challenges resulting from its fundamental architecture, particularly for high mass resolution analysis required for accurate and precise isotopologue ratio studies. The finite trap volume and narrow electrical potential window means that ion populations are susceptible to space charge effects. For molecular analysis this has little to no negative consequences and as long as ion loads are kept below recommended limits space charge related artifacts do not impact mass spectra used for molecular identification. For high precision quantification more care is needed as spectral artifacts can be subtle and only become apparent when evaluating the isotopologue ratio data. In general, these space charge related artifacts can be avoided by limiting the ion load in the trap. Utilizing the quadrupole mass filter to only transmit ions of interest to the analyzer is the best way to manage these effects while simultaneously maximizing counts on molecular ions of interest. In addition to spectral artifacts (i.e. artifacts originating in the Orbitrap itself) other analytical concerns exist similar to magnetic sector IRMS (Eiler, 2007; Eiler et al., 2020). Non-linearity and signal dependent changes in mass discrimination can occur but similar to classical approaches this is dealt with through sample standard bracketing and the principle of identical treatment.

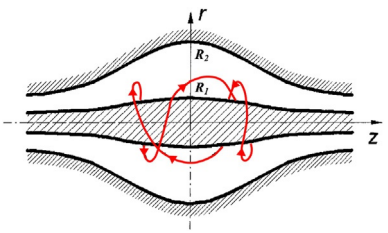

Fig. 12 Schematic of the Orbitrap analyzer slightly modified from Makarov (2000), including an example ion orbital trajectory. "R" denotes inner (R_1) and outer (R_2) electrode radii and "z" is the potential field symmetry axis. The frequency modes along this "z" axis are used for deriving m/z information. Slightly modified from Makarov A (2000) Electrostatic axially harmonic orbital trapping: A high performance technique of mass analysis. *Analytical Chemistry* 72(6): 1156–1162. PMID: PMID: 10740853.

Acquiring isotopologue information from a Hybrid Orbitrap MS

Mass analysis using a hybrid Orbitrap MS instruments consists of several steps. Ions are produced by a range of different ion sources. Here we focus on electron impact (EI) gas source and electrospray (ESI) liquid source experiments as they cover the majority of applications (1 in Fig. 13). RF lenses and ion transfer optics transmit ions, remove neutrals, and collisionally cool the ions (2, Fig. 13). The quadrupole (3, Fig. 13) determines the mass (m/z) range that is transmitted to the analyzer portion of the instrument. Based on the total ion current measured at the internal charge detector and the users target Orbitrap current, an injection time is determined that achieves consistent ion currents in the Orbitrap (4, Fig. 13). This ability to auto regulate ion load in the Orbitrap analyzer is called automatic gain control (AGC). The importance of AGC in reliable accurate isotopologue ratio measurements will be detailed in a later section. Ions are accumulated in either the Ion Routing Multipole or the C-trap depending on the instrument (5 and 6, Fig. 13). Ions are then injected via the C-trap into the Orbitrap analyzer, where they orbit the central electrode and oscillate axially in an intricate spiral, which produces an image current on the outer electrodes (7, Fig. 13). The sum of the image current frequency modes vs time is referred to as a transient, where the axial frequency (ω) for a given ion is defined as

$$\omega = \sqrt{\left(\frac{z}{m}\right)k}, \tag{12}$$

where k is the characteristic field curvature and (ω) is in the units (rad/s). The transients are interpreted via a Fast Fourier transform yielding a frequency spectrum called a scan (or microscan), which is converted to a mass spectrum using,

$$\frac{M}{\delta M} = \frac{1}{2}\left(\frac{\omega}{\delta\omega}\right) \tag{13}$$

and a locally acquired calibration. This process is then repeated to accumulate ion counts and improve the analytical error of the measurement. Details around experiment design and factors contributing to accuracy and precision are discussed in the following sections.

Considerations for designing measurement approaches

Sensitivity

Evaluation of sensitivity for an Orbitrap MS differs from that for magnetic sector instruments. For a magnetic sector instrument there is a relatively simple relationship between the number of molecules passing into the source and the resulting ion current measured at the detector. For an Orbitrap MS, on the other hand, ions are accumulated and injected in discrete packets for analysis, and so an additional term is required. This additional term is injection time, or the amount of time needed to reach a certain ion packet size at a given ion flux from the source. It is usually tens of milliseconds. The considerations in evaluating ion fluxes and the magnitude of the charge associated with an individual ion as detected by the Orbitrap analyzer are outlined in Makarov and Denisov (2009) and Eiler et al. (2017). The latter study deals almost exclusively with sensitivities measured on the EI source of the QExactive™ GC Orbitrap MS where sensitivity values on the order of 10,000 molecules per ion are reported. By contrast, ESI is a concentration-dependent ionization technique, which dictates that from the fixed amount of available charges in the source the mole fraction of the target analyte in solution dictates the sensitivity. In general for both approaches, when considering the amount

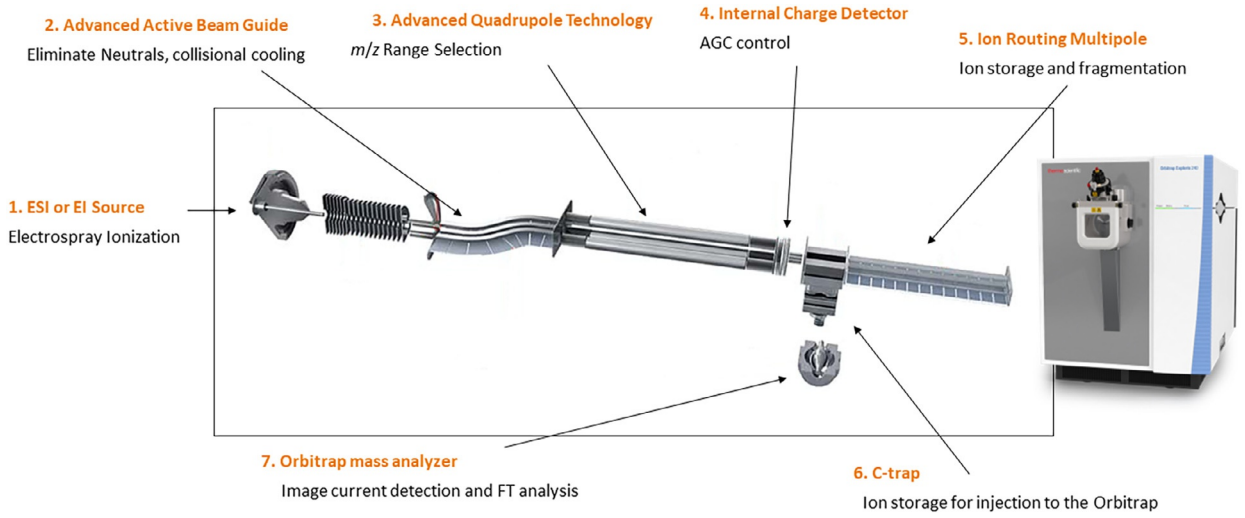

Fig. 13 Anatomy of the current Thermo Scientific Hybrid Orbitrap Exploris™ MS. Includes the significant components and functional descriptions for IRMS applications. Some components and functions are omitted as they are not significantly addressed in the text.

of sample needed to achieve subpermil precision on a given isotope ratio, Orbitrap approaches require low nanomole to picomole quantities of analyte compared to classical IRMS approaches, which often require micromoles of material.

Resolution and signal to noise

High-mass-resolution measurements of molecular ions is a key advantage of Orbitrap technologies (e.g., ^{13}C vs D vs ^{17}O, 2 × ^{13}C vs ^{18}O vs ^{34}S, etc.…). Due to the increasing resolution requirement for separation as the overall molecular mass increases, there are clear limits on how large a molecular ion can be while still achieving useful isotopologue separation (Fig. 14).

Higher resolution Orbitrap scans are achieved by increasing scan time. The longer an ion packet oscillates within the Orbitrap analyzer, the higher the precision of the determination of the frequency modes in the transient. This is an important consideration when designing measurement approaches as the time required for extremely high resolution can be significant. Resolution of 15,000 is achieved with a scan rate of 22 Hz, while a resolution of 480,000 is obtained at around 0.8 Hz. Therefore, when considering optimizing measurement time and sample utilization, the minimum required resolution is advantageous.

Another important parameter to optimize for obtaining the highest quality natural abundance isotopologue data is the signal to noise ratio. Orbitrap spectral noise is determined for each mass and resolution during data collection with a given frequency mode in the image current transient absent spectral features. It is advantageous to sum a number of transients prior to Fourier transform treatment as signal increases linearly, while noise only increases as the square route of the number of transients summed. This roughly equates to a signal to noise improvement of a factor 3 when going from single scans to 10 microscans. This results in significantly better accuracy and precision for natural abundance isotopologue ratio measurements.

It is tempting to think that simply increasing signal in the Orbitrap is the best solution for generating more ion counts and enabling faster, high precision measurements. However, there is a limit to the number of ions that can be simultaneously measured in the Orbitrap before space charge related aberrations degrade the quality of the analysis (Gorshkov et al., 2012). The most common effects are the combining or degradation of a small ion beam proximal to a large ion beam (e.g. degradation of the D beam near a large ^{13}C beam). The resulting behaviors can range from mass inaccuracy, unstable resolution, and complete destruction of the minor beam. Limiting Orbitrap fills to between 1×10^{-5} to 1×10^{-6} ions is ideal for avoiding space charge effects.

Fragmentation

Another advantage of the Hybrid Orbitrap MS platform is the ability to fragment molecular ions using energetic collisions. Fragmentation can be achieved in the ion transfer optics prior to the quadrupole, which allows quadrupole filtering of the produced fragments. Alternatively, similar fragmentation techniques can be executed in the ion routing multipole or HCD cell (for older generation instruments), after which all produced fragments are introduced to the Orbitrap analyzer. The ability to perform controlled, predictable fragmentation enables position specific isotopic distributions (similar to GC-Py-GC-C-IRMS) where specific functional groups can be cleaved from larger molecules (Weiss et al., 2023). In this way, a molecular average measurement can be made and compared to measurements of one or more fragments from the same analyte to piece together the site specific isotopic composition of the original molecule. This capability also provides the ability to measure isotopologue ratios of portions of much larger molecules, which would not otherwise be possible to due to mass resolution requirements of order hundreds of thousands at high mass (>300–400 m/z).

The so called "M + 1" experiments are another way to utilize the hybrid Orbitrap MS architecture to design unique experimental approaches (Fig. 15, adapted from Neubauer et al., 2018). By using the quadrupole to exclude the major, unsubstituted species the relative abundance difference between isotopically substituted species is decreased, while simultaneously amplifying the signal of each minor species. This is possible because the Orbitrap is being filled (based on the AGC target assignment) but excludes the

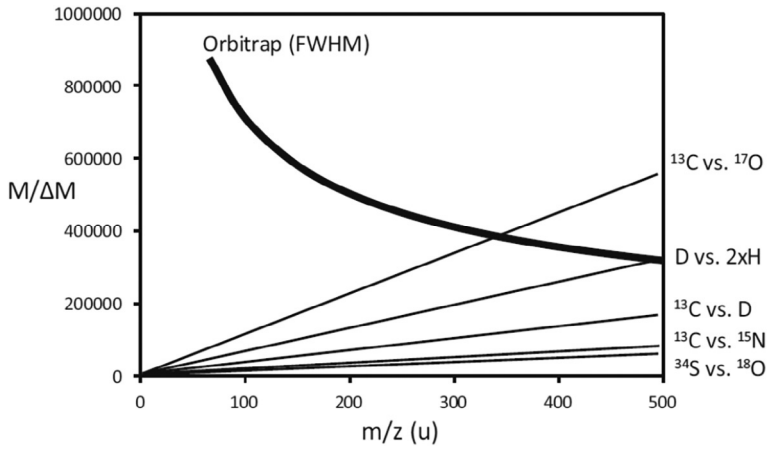

Fig. 14 Required resolution for isotopologue separations of interest from Eiler et al. (2020). The bold curve is a representation of the resolution vs *m/z* performance of an Orbitrap Exploris 480 MS. As resolution is a function of m/z, where frequency mode evolves as in Eq. (12), lower m/z targets achieve higher resolutions.

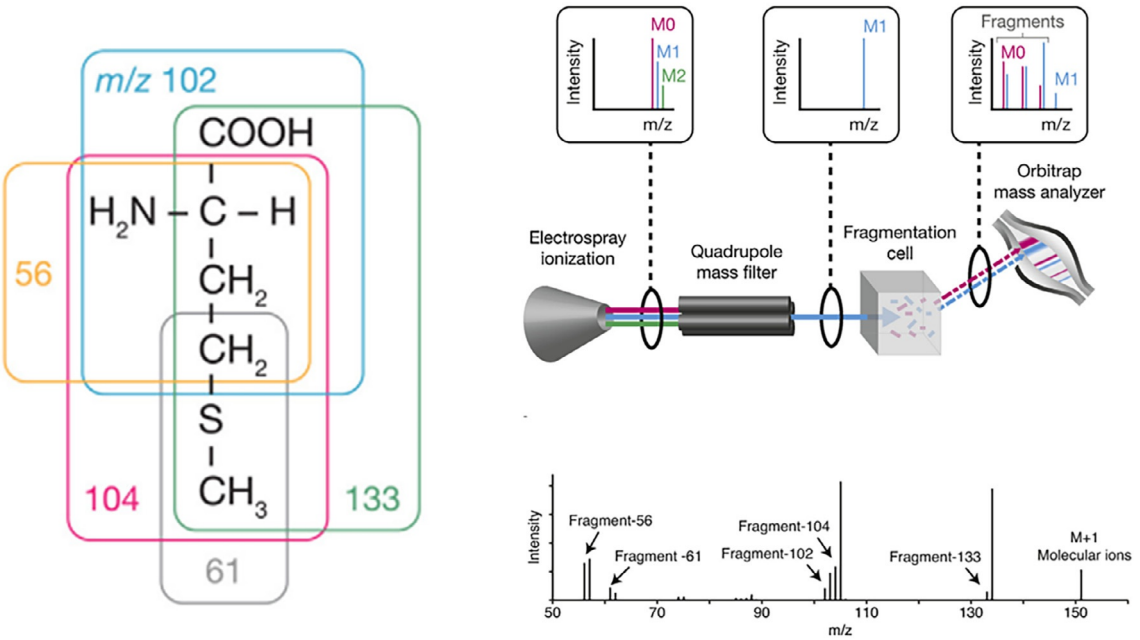

Fig. 15 Schematic of steps involved in a M + 1 fragmentation experiment of methionine molecular ions. Singly substituted M + 1 isotopologues are transferred through the quadrupole mass filter. The fragments and associated masses result from predictable bond ruptures at controlled collision energies with nitrogen gas molecules. Adapted from Neubauer C, Sweredoski MJ, Moradian A, Newman DK, Robins RJ, and Eiler JM (2018) Scanning the isotopic structure of molecules by tandem mass spectrometry. *International Journal of Mass Spectrometry* 434: 276–286.

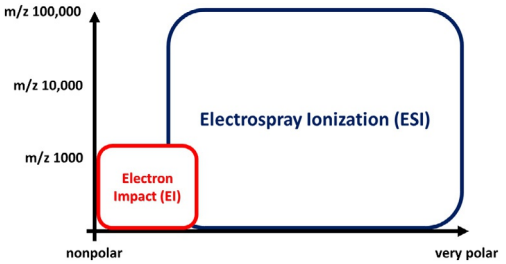

Fig. 16 Differences in polarity of target molecules determines what source type is most ideal for high sensitivity measurements. Non-polar and volatile compounds are best suited for GC sample introduction and electron impact ionization. ESI is the best source type to ensure efficient ionization of slightly to very polar compounds.

major, unsubstituted species. For oxy-anions and smaller molecules this can serve to amplify the multiply substituted species for higher precision measurements. For larger organics "M + 1" or "M + n" (where n = any integer mass above the unsubstituted molecular mass) molecular ions can then be fragmented and isotopic substitutions can be quantified in the fragments at relatively subequal abundances, increasing precision, decreasing resolution, and thus also decreasing measurement duration.

Example applications

Depending on the target analytes of interest, different source technologies are more or less suitable for ionization of different classes of molecules. One criterion for selecting suitable ionization techniques is the target molecule's polarity (Fig. 16). EI gas source instruments are ideal for analyzing room temperature gases (classical IRMS targets), non-polar molecules, which are readily volatilized, and refractory organics that can be liberated via pyrolysis. ESI source instruments can effectively ionize most molecules that can be dissolved in either water, methanol, acetonitrile, or a number of other solvents. Other less common source types can be operated on Hybrid Orbitrap MS systems, but for light stable isotope geochemistry, geobiology and biochemistry the EI or ESI ionization sources enable access to the majority of analytical targets.

By its nature, the Orbitrap analyzer has a limit on the number of ions that can be simultaneously analyzed, resulting in challenges when seeking highly precise and accurate natural abundance isotope ratio measurements. Strategies must be employed to mitigate this limitation, especially when a target's abundance distribution requires a large dynamic range. As with all analytical techniques, the precision of the measurement is ultimately limited by the stability of the system, including both the sample delivery hardware and the mass spectrometer itself. The Orbitrap MS has been repeatedly shown to operate just above shot noise limits for

exceedingly long measurement durations (Eiler et al., 2017; Csernica et al., 2023a). However, as with magnetic sector instruments, the challenges to acquiring highly accurate isotope ratio measurements are the efficacy of the sample/standard comparison technique, choices of reference materials, and the mass discrimination stability during the alternating sample/standard measurements. In what follows we describe Orbitrap hardware configurations suitable for different applications, together with discoveries enabled by these systems.

Electron impact source sample introduction

The Hybrid Orbitrap GC instruments are fitted with an EI source that can also use reagent gas for chemical ionization (CI). In normal operation the sample gas arrives entrained in He eluting from a GC column. The standard configuration can support IRMS experiments utilizing the "direct elution" approach (Eiler et al., 2017; Zeichner et al., 2022, 2023a,b). This style of analysis enables the user to measure isotope ratios from any number of compounds separated by the GC column. However, precision is significantly limited due to the short duration of the eluting GC peak and the resulting limited number of Orbitrap scans (Zeichner et al., 2022). Standardization is accomplished by injecting compounds of interest with known isotopic composition (characterized by GC-IRMS) in alternating injections with the unknowns. This method has been successfully applied to fragment ions of serine and PAHs in meteorite extracts, and most recently extracts from the asteroid Ryugu (Zeichner et al., 2022, 2023a,b). Results showed that clumping of ^{13}C ($2 \times {}^{13}C$) in PAHs requires formation of these materials at such low temperatures that they must be inherited from the interstellar medium.

When more sample material is available, GC peak broadening proves to be an advantage because longer elution times result in more scans and therefore better precision (Eiler et al., 2017; Hofmann et al., 2020; Chimiak et al., 2021). In this approach, switching valves direct flow between a "direct elution" path to the MS and a "peak broadening reservoir" path to the MS. The later contains an expansion volume of a certain size, tuned to achieve the desired elution time when a single peak is diverted, diluted and flushed to the MS. This approach is well suited for site-specific analyses at relatively high precision of derivatized amino acids, aromatic hydrocarbons (Chimiak et al., 2021; Hofmann et al., 2020) and other volatile organic molecules (e.g. ethyle toluene, Cesar et al., 2019). These "peak broadening" measurements, in contrast to the "direct elution" approach, are extended from seconds to tens of minutes and therefore improve on the precision by about an order of magnitude. Sub ‰ carbon and sub 5 ‰ hydrogen isotope measurements are possible using peak broadening. Continued work on these topics has the potential to identify biomarkers and record synthesis and maturation mechanisms of planetary and terrestrial organics (e.g., Zeichner et al., 2023a,b).

Open split and dual inlet style sample introduction techniques are also possible on the EI source Hybrid Orbitrap instruments (Eiler et al., 2017). These approaches, while not prevalent in the literature, have the potential to yield the highest precision measurements for room temperature gases or gases evolved from liquids or solids in a controlled manner. Due to the Orbitrap analyzer's ability measure at shot noise limits for extended periods of time, either of these gas introduction techniques that can deliver stable repeatable measurement cycles in-definitely, could produce measurements with on order 0.01‰ precision.

Electrospray liquid sample introduction

ESI Orbitrap MS effectively ionizes a broad range of molecules from only slightly polar to extremely polar and can be coupled to either a dual syringe inlet or an HPLC for sample and standard solution delivery (Fig. 16). This allows the same system to make routine isotopologue ratio measurements of small oxyanions (Neubauer et al., 2018; Csernica et al., 2023a; Hilkert et al., 2021), small organics like acetate (Mueller et al., 2022), underivatized amino acids (Neubauer et al., 2018; Hofmann et al., 2020; Csernica et al., 2023a,b; Weiss et al., 2023) and fragments of larger organic molecules with m/z greater than 300.

ESI ionization is a "soft" ionization technique and does not generate fragments in the same way that EI does. Molecules are ionized via charge transfer in the liquid phase and solvent is evaporated as the fine droplets travel along a high voltage potential. Finally, gas-phase molecular ions are transferred into the MS for analysis. The ability to measure isotopologue ratios of intact oxy-anions provides a new and unique perspective with additional isotopic dimensions (Fig. 17) (Neubauer et al., 2018; Csernica et al., 2023a; Hilkert et al., 2021). In addition to the added isotopologue dimensions, ESI Orbitrap analyses adds 1–2 (sometimes more) orders of magnitude of sensitivity compared to other approaches. So, rather than requiring nanomoles to micromoles of analyte, sub ‰ measurements can be done on picomols of sample. An advantage of ESI ionization is a certain degree of matrix tolerance and the ability to use additives to stabilize the source chemistry, speciation, and mass discrimination (Hilkert et al., 2021). This enables some targets to be measured in mixtures without pre-purification. This matrix tolerance provides the ability to utilize "dilute and shoot" and dual inlet style sample introduction techniques with less precise matching of sample and standard matrix chemistry.

Mueller et al. (2022) show that acetate carbon and hydrogen isotopes can be measured simultaneously from samples sizes 50 to 1000× less using ESI Orbitrap MS than with classical approaches and with arguably better precision. This study reported large differences in fractionation for both carbon and hydrogen isotopes associated with acetate produced by autotrophic acetogens vs fermentors. The sensitivity of this measurement provides a new and unique capability for understanding microbial metabolisms in situ, in environments like marine pore waters where concentrations can be exceedingly low.

Although extending beyond the realm of geochemistry, per se, Kuhlbusch et al. (2023) has shown that caffeine can be isolated from soft drinks and measured at high resolution (240 k, Fig. 18) using HPLC peak capture and on-line referencing techniques. The HPLC separation alleviates matrix effects for better accuracy, while the peak capture provides longer, higher precision measurements

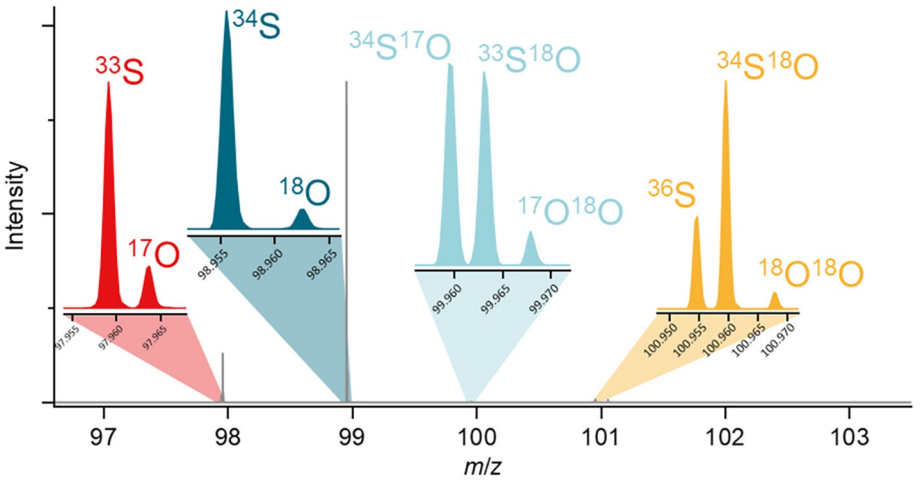

Fig. 17 Isotopologue spectrum of isotopically substituted sulfate molecular ions. Note, integer masses correspond to HSO_4^- ions with rare isotope substitutions as peak labels. Measuring intact molecular ions provides the opportunity to measure 5 isotopically "clumped" species in addition to all 3 oxygen and 4 sulfur species. The unsubstituted peak is not shown. Courtesy of Thermo Fischer Scientific.

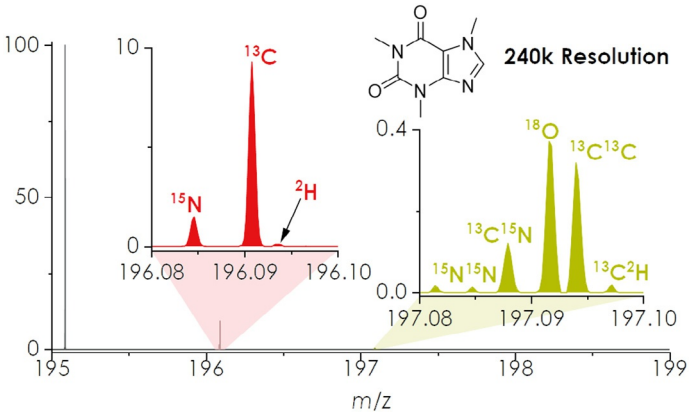

Fig. 18 Isotopologue spectrum of caffeine collected at 240 k resolution. Simultaneous acquisition of all isotopologues provides sub ‰ precision for ^{13}C and ^{15}N, sub 2 ‰ for ^{18}O, and sub 5 ‰ for D/H.

similar to the GC "peak broadening" approach. The on-line referencing technique allows the purified compound eluting from the column to be compared to a pure standard during an automated measurement, and eliminates the need for off-line sample preparation.

Most of the studies described above benchmark the new Orbitrap-IRMS measurements against classical IRMS techniques to demonstrate accuracy. As of this writing, Weiss et al. (2023) provides the most thorough benchmarking of Orbitrap-PSIA-IRMS measurements of alanine against bulk EA-IRMS, GC-C-IRMS, and GC-Py-GC-C-IRMS. This study provides an exhaustive comparison of sample size, measurement duration (identified as the main advantage), and accuracy and precision, and also verifies fragmentation patterns using labelled standard material. Another important take away is the limitation imposed by reduced sensitivity for m/z below 50. This needs to be considered when generating fragmentation strategies for PSIA on the ESI-Orbitrap MS instruments.

Summary and outlook

Double-focusing magnetic-sector mass spectrometers provide for high-precision isotopologue ratio measurements for relatively low-mass molecular species. Advantages of these methods are the exploitation of rapid sample/standard switching to account for instrumental effects and the relatively straightforward sample introduction. These tools are now well developed for studies of "clumped" isotopes in gases. High-precision measurements of isotopologue ratios involving multiply-substituted (clumped) species generally requires on the order of tens of micromoles of gas. Measurements of site-specific isotope ratios are indirect, involving cleaving of molecules in electron impact sources, and are thus limited with this technology. However, there are other

measurements of fragments made possible with HR-IRMS instruments that will likely prove useful in the future. For example, the triple oxygen isotopic composition of CO_2, notoriously difficult because of the irresolvable mass interference between ^{13}C and ^{17}O, is possible using the O^+ fragment from CO_2^+ due to the ability to resolve mass interferences (e.g., OH^+ from O^+), providing a greatly streamlined means of measuring $\Delta^{17}O$ in carbon dioxide gases (e.g., Adnew et al., 2019). The large-geometry instrument with D/X of ~1400 is probably the maximum size that is practical for the near future. Further improvements in mass resolution and sensitivity will likely come from continued advancements in ionization sources, transfer optics, and collector technologies.

Compared with double-focussing mass-sector instruments, Orbitrap Fourier-transform IRMS provides an order of magnitude greater mass resolution on a larger number of species measured simultaneously. It also offers greater sensitivity with samples typically in the nanomole to picomole range. In many cases, these advantages come at the cost of precision in isotopologue ratio measurement. While this technology is especially well-suited for studies of organic compounds, it is being used increasingly for simpler species of geochemical interest as well. New techniques, such as emulating the sample/standard dual inlet designs of magnetic-sector instruments, should continue to improve the precision of Orbitrap Fourier-transform mass spectrometry methods for isotopologue ratio analysis. The ability of these instrument platforms to simultaneously acquire information on the relative abundances of large (5–100) numbers of isotopologues will require different approaches to measurement design, data treatment, and predictive simulations.

While not the subject of this chapter, it would be a glaring omission to not mention advances in tunable infrared laser direct absorption spectroscopy (TILDAS) (e.g., Ono et al., 2014; Perdue et al., 2022) and cavity ring-down laser spectrometry (CRDS) (e.g., Steig et al., 2014) as increasingly important methods for measuring isotopologues of molecules of geochemical significance. These spectroscopic techniques are providing the means for rapid analyses of isotopologue ratios of gases with precision in some cases (e.g., for CO_2) rivaling magnetic-sector IRMS methods. Applications include clumped isotopes of methane measured by TILDAS (Ono et al., 2014; Gonzalez et al., 2019), CO_2 clumping measured by TILDAS (Wang et al., 2020), TILDAS measurements of triple-oxygen isotopes (i.e., $\Delta'^{17}O$) free from interferences from carbon isotopes (Perdue et al., 2022), TILDAS measurements of isotope clumping in N_2O produced by bacterial denitrification (Kantnerová et al., 2022), and position-specific $^{13}C/^{12}C$ for propane using TILDAS (Nataraj et al., 2023). Limitations of these methods at present are the large gas samples required for analysis of rare, multiply-substituted species (e.g., $^{12}CH_2D_2$, but see Prokhorov and Mohn, 2022), and the infrared inactivity of homonuclear diatomic molecules (e.g., N_2).

All of these technologies have led to a substantial increase in the information content of isotope distributions in molecular species. Applications include the isotopologue abundances of CO_2, CH_4 and other alkanes, CH_3, N_2, O_2, H_2, N_2O, and SO_4, as well as site-specific isotope ratios for larger molecules, including amino acids, aromatic hydrocarbons, and PAH's, among others.

References

Adnew GA, Hofmann ME, Paul D, Laskar A, Surma J, Albrecht N, Pack A, Schwieters J, Koren G, Peters W, and Röckmann T (2019) Determination of the triple oxygen and carbon isotopic composition of CO_2 from atomic ion fragments formed in the ion source of the 253 ultra high-resolution isotope ratio mass spectrometer. *Rapid Communications in Mass Spectrometry* 33(17): 1363–1380.

Affek HP, Bar-Matthews M, Ayalon A, Matthews A, and Eiler JM (2008) Glacial/interglacial temperature variations in Soreq cave speleothems as recorded by ``clumped isotope" thermometry. *Geochimica et Cosmochimica Acta* 72(22): 5351–5360. https://doi.org/10.1016/j.gca.2008.06.031.

Affek HP and Eiler JM (2006) Abundance of mass 47 CO_2 in urban air, car exhaust, and human breath. *Geochimica et Cosmochimica Acta* 70(1): 1–12.

Affek HP and Xu X (2007) Seasonal and diurnal variations of $^{13}C^{18}O^{16}O$ in air: Initial observations from Pasadena, CA. *Geochimica et Cosmochimica Acta* 71(21): 5033–5043. https://doi.org/10.1016/j.gca.2007.08.014.

Ash J, Egger M, Treude T, Kohl I, Cragg B, Parkes R, Slomp C, Sherwood Lollar B, and Young ED (2019) Exchange catalysis during anaerobic methanotrophy revealed by $^{12}CH_2D_2$ and $^{13}CH_3D$ in methane. *Geochemical Perspectives Letters*: 26–30.

Bajnai D, Guo W, Spötl C, Coplen TB, Methner K, Löffler N, Krsnik E, Gischler E, Hansen M, Henkel D, et al. (2020) Dual clumped isotope thermometry resolves kinetic biases in carbonate formation temperatures. *Nature Communications* 11(1): 4005.

Brenninkmeijer CAM and Röckmann T (1999) Mass spectrometry of the intramolecular nitrogen isotope distribution of environmental nitrous oxide using fragment-ion analysis. *Rapid Communications in Mass Spectrometry* 13(20): 2028–2033.

Cao X, Bao H, and Peng Y (2019) A kinetic model for isotopologue signatures of methane generated by biotic and abiotic CO_2 methanation. *Geochemica et Cosmochimica Acta* 249: 59–75.

Cesar J, Eiler J, Dallas B, Chimiak L, and Grice K (2019) Isotope heterogeneity in ethyltoluenes from australian condensates, and their stable carbon site-specific isotope analysis. *Organic Geochemistry* 135: 32–37.

Chimiak L, Elsila J, Dallas B, Dworkin J, Aponte J, Sessions A, and Eiler J (2021) Carbon isotope evidence for the substrates and mechanisms of prebiotic synthesis in the early solar system. *Geochimica et Cosmochimica Acta* 292: 188–202.

Clog M, Lawson M, Peterson B, Ferreira AA, Santos Neto EV, and Eiler JM (2018) A reconnaissance study of $^{13}C-^{13}C$ clumping in ethane from natural gas. *Geochimica et Cosmochimica Acta* 223: 229–244.

Cross WG (1951) Two-directional focusing of charged particles with a sector-shaped, uniform magnetic field. *Review of Scientific Instruments* 22(10): 717–722.

Csernica T, Bhattacharjee S, and Eiler J (2023a) Accuracy and precision of esi-orbitrap-irms observations of hours to tens of hours via reservoir injection. *International Journal of Mass Spectrometry* 490: 117084.

Csernica T, Sessions AL, and Eiler JM (2023b) High-dimensional isotomics, part 2: Observations of over 100 constraints on methionine's isotome. *Chemical Geology* 642: 121771.

Douglas PMJ, Stolper DA, Smith DA, Walter Anthony KM, Paull CK, Dallimore S, Wik M, Crill PM, Winterdahl M, Eiler JM, and Sessions AL (2016) Diverse origins of Arctic and Subarctic methane point source emissions identified with multiply-substituted isotopologues. *Geochimica et Cosmochimica Acta* 188: 163–188.

Dempster AJ (1935) New methods in mass spectrometry. *Proceedings of the American Philosophical Society* 75: 755–767.

Douglas PMJ, Stolper DA, Eiler JM, Sessions AL, Lawson M, Shuai Y, Bishop A, Podlaha OG, Ferreira AA, Santos Neto EV, Niemann M, Steen AS, Huang L, Chimiak L, Valentine DL, Fiebig J, Luhmann AJ, Seyfried WE, Etiope G, Schoell M, Inskeep WP, Moran JJ, and Kitchen N (2017) Methane clumped isotopes: Progress and potential for a new isotopic tracer. *Organic Geochemistry* 113.

Eiler JM (2007) "Clumped-isotope" geochemistry - The study of naturally-occurring, multiply-substituted isotopologues. *Earth and Planetary Science Letters* 262(3–4): 309–327.

Eiler JM and Schauble E (2004) $^{18}O^{13}C^{16}O$in Earths atmosphere. *Geochimica et Cosmochimica Acta* 68: 4767–4777.

Eiler JM, Ghosh P, Affek H, Schauble E, Adkins J, Schrag D, and Hoffman P (2005) Carbonate plaeothermometry based on abundances of ^{13}C–^{18}O bonds. In: *Goldschmidt Conference, Moscow, Idaho*, p. A127. Cambridge Publications.

Eiler JM, Clog M, Magyar P, Piasecki A, Sessions A, Stolper D, Deerberg M, Schlueter H-J, and Schwieters J (2013) A high-resolution gas-source isotope ratio mass spectrometer. *International Journal of Mass Spectrometry* 335: 45–56.

Eiler J, Cesar J, Chimiak L, Dallas B, Grice K, Griep-Raming J, Juchelka D, Kitchen N, Lloyd M, Makarov A, Robins R, and Schwieters J (2017) Analysis of molecular isotopic structures at high precision and accuracy by orbitrap mass spectrometry. *International Journal of Mass Spectrometry* 422: 126–142.

Eiler JM, Griep-Raming J, Juchela D, and Makarov A (2020) *Analysis of molecular isotopic structure by Fourier-Transform Mass Spectrometry*, pp. 1–32. Singapore: Springer Nature Singapore.

Etiope G (2017) Methane origin in the Samail ophiolite: Comment on "Modern water/rock reactions in Oman hyperalkaline peridotite aquifers and implications for microbial habitability" [Geochem. Cosmochim. Acta 179 (2016) 217-24]. *Geochemica et Cosmochimica Acta* 197: 467–470.

Fiebig J, Bajnai D, Loffler N, Methner K, Krsnik E, Mulch A, and Hofmann S (2019) Combined high-precision Δ_{48} and Δ_{47} analysis of carbonates. *Chemical Geology* 522: 186–191.

Giunta T, Young ED, Warr O, Kohl I, Ash JL, Martini A, Mundle SOC, Rumble D, Pérez-Rodríguez I, Wasley M, LaRowe DE, Gilbert A, and Sherwood Lollar B (2019) Methane sources and sinks in continental sedimentary systems: New insights from paired clumped isotopologues $^{13}CH_3D$ and $^{12}CH_2D_2$. *Geochimica et Cosmochimica Acta* 245: 327–351.

Ghosh P, Adkins J, Affek H, Balta B, Guo W, Schauble EA, Schrag D, and Eiler JM (2006a) 13C-18O bonds in carbonate minerals: A new kind of paleothermometer. *Geochimica et Cosmochimica Acta* 70: 1439–1456.

Ghosh P, Eiler J, Campana SE, and Feeney RF (2007) Calibration of the carbonate "clumped isotope" paleothermometer for otoliths. *Geochimica et Cosmochimica Acta* 71(11): 2736–2744. https://doi.org/10.1016/j.gca.2007.03.015.

Ghosh P, Garzione CN, and Eiler JM (2006b) Rapid uplift of the altiplano revealed through ^{13}C-^{18}O bonds in paleosol carbonates. *Science* 311(5760): 511–515. https://doi.org/10.1126/science.1119365.

Giunta T, Young ED, Labidi J, Sansjofre P, Jézéquel D, Donval J-P, Brandily C, and Ruffine L (2022) Extreme methane clumped isotopologue bio-signatures of aerobic and anaerobic methanotrophy: Insights from the Lake Pavin and the Black Sea sediments. *Geochemica et Cosmochimica Acta* 338: 34–53.

Gonzalez Y, Nelson DD, Shorter JH, McManu BJ, Dyroff C, Formolo M, Wang DT, Western CM, and Ono S (2019) Precise measurements of $^{12}CH_2D_2$ by Tunable Infrared Laser Direct Absorption Spectroscopy. *Analytical Chemistry* 91: 14967–14974.

Gorshkov MV, Fornelli L, and Tsybin YO (2012) Observation of ion coalescence in orbitrap Fourier transform mass spectrometry. *Rapid Communications in Mass Spectrometry* 26(15): 1711–1717.

Gosh P, Eiler J, Adkins J, Balta B, Schauble E, Wanamaker A, Introne C, and Kreutz K (2004) Ratio of multi-substituted isotopologues in natural carbonates, a novel tool to study palaeo temperature. In: *EOS Trans. AGU, Fall Meet. Suppl., San Francisco, pp. Abstract P11A–0554*.

Gruen DS, Wang DT, Könneke M, Topçuoğlu BD, Stewart LC, Gold-hammer T, Holden JF, Hinrichs K-U, and Ono S (2018) Experimental investigation on the controls of clumped isotopologue and hydrogen isotope ratios in microbial methane. *Geochimica et Cosmochimica Acta* 237: 339–356.

Guo W and Eiler JM (2007) Temperatures of aqueous alteration and evidence for methane generation on the parent bodies of the CM chondrites. *Geochemica et Cosmochimica Acta* 71: 5565–5575.

Haghnegahdar MA, Schauble EA, and Young ED (2017) A model for $^{12}CH_2D_2$ and $^{13}CH_3D$ as complementary tracers for the budget of atmospheric CH_4. *Global Biogeochemical Cycles* 31(9): 1387–1407.

Haghnegahdar MA, Sun J, Hultquist N, Hamovit ND, Kitchen N, Eiler J, Ono S, Yarwood SA, Kaufman AJ, Dickerson RR, Bouyon A, Magen C, and Farquhar J (2023) Tracing sources of atmospheric methane using clumped isotopes. *Proceedings of the National Academy of Science* 120(47): e2305574120.

He B, Olack GA, and Colman AS (2012) Pressure baseline correction and high-precision CO_2 clumped-isotope (Δ_{47}) measurements in bellows and micro-volume modes. *Rapid Communications in Mass Spectrometry* 26(24): 2837–2853.

Hilkert A, Bhlke JK, Mroczkowski SJ, Fort KL, Aizikov K, Wang XT, Kopf SH, and Neubauer C (2021) Exploring the potential of electrospray-orbitrap for stable isotope analysis using nitrate as a model. *Analytical Chemistry* 93(26): 9139–9148. PMID: 34165950.

Hofmann AE, Chimiak L, Dallas B, Griep-Raming J, Juchelka D, Makarov A, Schwieters J, and Eiler JM (2020) Using orbitrap mass spectrometry to assess the isotopic compositions of individual compounds in mixtures. *International Journal of Mass Spectrometry* 457: 116410.

Ireland T (2014) 15.21 - ion microscopes and microprobes. In: Holland HD and Turekian KK (eds.) *Treatise on Geochemistry*, 2nd edn, pp. 385–409. Oxford: Elsevier.

Johnson EG and Nier AO (1953) Angular aberrations in sector shaped electromagnetic lenses for focusing beams of charged particles. *Physical Review* 91(1): 10–17. https://doi.org/10.1103/PhysRev.91.10.

Kantnerová K, Hattori S, Toyoda S, Yoshida N, Emmenegger L, Bernasconi SM, and Mohn J (2022) Clumped isotope signatures of nitrous oxide formed by bacterial denitrification. *Geochimica et Cosmochimica Acta* 328: 120–129.

Kingdon KH (1923) A method for the neutralization of electron space charge by positive ionization at very low gas pressures. *Physics Review* 21: 408–418.

Kuhlbusch N, Kohl I, Juchelka D, Hayen H, and Hilkert A (2023) Isotopologue ratio analysis in organic compounds using ESI-FTMS: Origin of caffeine in foods. *GASIR* 2023.

Labidi J and Young E (2022) The origin and dynamics of nitrogen in the earth's mantle constrained by $^{15}N^{15}N$ in hydrothermal gases. *Chemical Geology* 591: 120709.

Labidi J, Barry PH, Bekaert DV, Broadley MW, Marty B, Giunta T, Warr O, Sherwood Lollar B, Fischer TP, Avice G, Caracausi A, Ballentine CJ, Halldórsson SA, Stefánsson A, Kurz MD, Kohl IE, and Young ED (2020) Hydrothermal $^{15}N^{15}N$ abundances constrain the origins of mantle nitrogen. *Nature* 580(7803): 367–371.

Labidi J, Young E, Fischer T, Barry P, Ballentine C, and de Moor J (2021) Recycling of nitrogen and light noble gases in the central American subduction zone: Constraints from $^{15}N^{15}N$. *Earth and Planetary Science Letters* 571: 117112.

Laskar AH, Peethambaran R, Adnew GA, and Rckmann T (2019) Measurement of $^{18}O^{18}O$ and $^{17}O^{18}O$ in atmospheric O_2 using the 253 ultra mass spectrometer and applications to stratospheric and tropospheric air samples. *Rapid Communications in Mass Spectrometry* 33(11): 981–994.

Lewis GN and Cornish RE (1933) Separation of the isotopic forms of water by fractional distillation. *Journal of the American Chemical Society* 55(6): 2616–2617.

Liu J, Harris RL, Ash JL, Ferry JG, Krause SJE, Labidi J, Prakash D, Sherwood Lollar B, Treude T, Warr O, and Young ED (2023) Reversibility controls on extreme methane clumped isotope signatures from anaerobic oxidation of methane. *Geochimica et Cosmochimica Acta* 348: 165–186.

Liu J, Treude T, Abbasov OR, Baloglanov EE, Aliyev AA, Harris CM, Leavitt WD, and Young ED (2024) Clumped isotope evidence for microbial alteration of thermogenic methane in terrestrial mud volcanoes. *Geology* 52(1): 22–26.

Lloyd MK, Eldridge DL, and Stolper DA (2021) Clumped $^{13}CH_2D$ and $^{12}CHD^2$ compositions of methyl groups from wood and synthetic monomers: Methods, experimental and theoretical calibrations, and initial results. *Geochim ica et Cosmochimica Acta* 297: 233–275.

Lloyd MK, Stein RA, Ibarra DE, Barclay RS, Wing SL, Stahle DW, Dawson TE, and Stolper DA (2023) Isotopic clumping in wood as a proxy for photorespiration in trees. *Proceedings of the National Academy of Sciences* 120(46): e2306736120.

Lucarelli JK, Carroll HM, Ulrich RN, Elliott BM, Coplen TB, Eagle RA, and Tripati A (2023) Equilibrated gas and carbonate standard-derived dual (Δ_{47} and Δ_{48}) clumped isotope values. *Geochemistry, Geophysics, Geosystems* 24(2): e2022GC010458.

Magyar PM, Orphan VJ, and Eiler JM (2016) Measurement of rare isotopologues of nitrous oxide by high-resolution multi-collector mass spectrometry. *Rapid Communications in Mass Spectrometry* 30(17): 1923–1940.

Makarov A (2000) Electrostatic axially harmonic orbital trapping: A high performance technique of mass analysis. *Analytical Chemistry* 72(6): 1156–1162. PMID: 10740853.

Makarov A and Denisov E (2009) Dynamics of ions of intact proteins in the orbitrap mass analyzer. *Journal of the American Society for Mass Spectrometry* 20(8): 1486–1495. PMID: 19427230.

Makarov A, Denisov E, Kholomeev A, Balschun W, Lange O, Strupat K, and Horning S (2006) Performance evaluation of a hybrid linear ion trap/orbitrap mass spectrometer. *Analytical Chemistry* 78(7): 2113–2120. PMID: 16579588.

Mangenot X, Xie H, Crémière A, Giunta T, Lilley M, Sissmann O, Orphan V, Schimmelmann A, Gaucher EC, Girard J-P, et al. (2023) ^{2}H-^{2}H clumping in molecular hydrogen method and preliminary results. *Chemical Geology* 621: 121278.

Matsuda H (1974) Double focusing mass spectrometers of second order. *International Journal of Mass Spectrometry and Ion Physics* 14(2): 219–233.

Matsuda H (1990) High-performance mass spectrometers of third-order focusing. *Nuclear Instruments and Methods in Physics Research Section A: Accelerators, Spectrometers, Detectors and Associated Equipment* 298(1): 199–204.

McKinney CR, McCrea JM, Epstein S, Allen HA, and Urey HC (1950) Improvements in mass spectrometers for the measurement of small differences in isotope abundance ratios. *The Review of Scientific Instruments* 21(8): 724–730.

Mueller EP, Sessions AL, Sauer PE, Weiss GM, and Eiler JM (2022) Simultaneous, high-precision measurements of δ^{2}H and δ^{13}C in nanomole quantities of acetate using electrospray ionization-quadrupole-orbitrap mass spectrometry. *Analytical Chemistry* 94(2): 1092–1100. PMID: 34967622.

Nataraj A, Tuzson B, Gianella M, Prokhorov I, Li G, Ebert V, Faist J, and Emmenegger L (2023) Position-specific isotope analysis of propane by mid-ir laser absorption spectroscopy. *Analytical Chemistry* 95(12): 5354–5361.

Neubauer C, Sweredoski MJ, Moradian A, Newman DK, Robins RJ, and Eiler JM (2018) Scanning the isotopic structure of molecules by tandem mass spectrometry. *International Journal of Mass Spectrometry* 434: 276–286.

Nier AO (1947) A mass spectrometer for isotope and gas analysis. *Review of Scientific Instruments* 18(6): 398–411.

Nier AO (1953) A double-focussing mass spectrometer. *National Bureau of Standards Circular (U.S.)* 522: 29–36.

Nothaft DB, Templeton AS, Rhim JH, Wang DT, Labidi J, Miller HM, Boyd ES, Matter JM, Ono S, Young ED, Kopf SH, Kelemen PB, Conrad ME, and T. O. D. P. S. Team (2021) Geochemical, biological, and clumped isotopologue evidence for substantial microbial methane production under carbon limitation in serpentinites of the samail ophiolite, Oman. *Journal of Geophysical Research: Biogeosciences* 126(10): e2020JG006025.

Ono S, Wang DT, Gruen DS, Sherwood Lollar B, Zahniser MS, McManus BJ, and Nelson DD (2014) Measurement of a doubly substituted methane isotopologue, $^{13}CH_3D$, by tunable infrared laser direct absorption spectroscopy. *Analytical Chemistry* 86(13): 6487–6494.

Ono S, Rhim JH, and Ryberg EC (2022) Rate limits and isotopologue fractionations for microbial methanogenesis examined with combined pathway protein cost and isotopologue flow network models. *Geochimica et Cosmochimica Acta* 325: 296–315.

Ostrom NE and Ostrom PH (2017) Mining the isotopic complexity of nitrous oxide: A review of challenges and opportunities. *Biogeochemistry* 132(3): 359–372.

Perdue N, Sharp Z, Nelson D, Wehr R, and Dyroff C (2022) A rapid high-precision analytical method for triple oxygen isotope analysis of CO_2 gas using tunable infrared laser direct absorption spectroscopy. *Rapid Communications in Mass Spectrometry* 36(21): e9391.

Petersen SV, Defliese WF, Saenger C, Da'Ron M, Huntington KW, John CM, Kelson JR, Bernasconi SM, Colman AS, Kluge T, Olack GA, Schauer AJ, Bajnai D, Bonifacie M, Breitenbach SFM, Fiebig J, Fernandez AB, Henkes GA, Hodell D, Katz A, Kele S, Lohmann KC, Passey BH, Peral MY, Petrizzo DA, Rosenheim BE, Tripati A, Venturelli R, Young ED, and Winkelstern IZ (2019) Effects of improved 17o correction on interlaboratory agreement in clumped isotope calibrations, estimates of mineral specific offsets, and temperature dependence of acid digestion fractionation. *Geochemistry, Geophysics, Geosystems* 20(7): 3495–3519.

Petrizzo DA and Young ED (2014) High-precision determination of ^{13}C–^{18}O bonds in CO_2 using multicollector peak hopping. *Rapid Communications in Mass Spectrometry* 28(11): 1185–1193.

Popa ME, Paul D, Janssen C, and Röckmann T (2019) H_2 clumped isotope measurements at natural isotopic abundances. *Rapid Communications in Mass Spectrometry* 33(3): 239–251.

Prokhorov I and Mohn J (2022) Cleanex: A versatile automated methane preconcentration device for high-precision analysis of $^{13}CH_4$, $^{12}CH_3D$, and $^{13}CH_3D$. *Analytical Chemistry* 94(28): 9981–9986.

Richet P, Bottinga Y, and Javoy M (1977) A review of hydrogen, carbon, nitrogen, oxygen, sulphur, and chlorine stable isotope fractionation among gaseous molecules. *Annual Reviews in Earth and Planetary Science* 5: 65–110.

Rittenberg D, Bleakney W, and Urey HC (1934) The equilibrium between the three hydrogens. *The Journal of Chemical Physics* 2(1): 48–49.

Röckmann T, Popa ME, Krol MC, and Hofmann MEG (2016) Statistical clumped isotope signatures. *Scientific Reports* 6(1): 31947.

Schauble EA, Ghosh P, and Eiler JM (2006) Preferential formation of 13C-18O bonds in carbonate minerals, estimated using first-principles lattice dynamics. *Geochimica et Cosmochimica Acta* 70: 2510–2529.

Schrenk MO, Brazelton WJ, and Lang SQ (2013) Serpentinization, carbon, and deep life. *Reviews in Mineralogy and Geochemistry* 75(1): 575–606.

Steig EJ, Gkinis V, Schauer AJ, Schoenemann SW, Samek K, Hoffnagle J, Dennis KJ, and Tan SM (2014) Calibrated high-precision ^{17}o-excess measurements using cavity ring-down spectroscopy with laser-current-tuned cavity resonance. *Atmospheric Measurement Techniques* 7(8): 2421–2435.

Stolper DA, Lawson M, Davis CL, Ferreira AA, Neto EVS, Ellis GS, Lewan MD, Martini AM, Tang Y, Schoell M, Sessions AL, and Eiler JM (2014) Formation temperatures of thermogenic and biogenic methane. *Science* 344(6191): 1500–1503.

Stolper DA, Martini AM, Clog M, Douglas PM, Shusta SS, Valentine DL, Sessions AL, and Eiler JM (2015) Distinguishing and understanding thermogenic and biogenic sources of methane using multiply substituted isotopologues. *Geochimica et Cosmochimica Acta* 161: 219–247.

Sutka RL, Ostrom NE, Ostrom PH, Breznak JA, Gandhi H, Pitt AJ, and Li F (2006) Distinguishing nitrous oxide production from nitrification and denitrification on the basis of isotopomer abundances. *Applied and Environmental Microbiology* 72(1): 638–644.

Taenzer L, Labidi J, Masterson AL, Feng X, Rumble D, Young ED, and Leavitt WD (2020) Low ΔCH_2D_2 values in microbialgenic methane result from combinatorial isotope effects. *Geochimica et Cosmochimica Acta* 285: 225–236.

Taguchi K, Gilbert A, Sherwood Lollar B, Giunta T, Boreham CJ, Liu Q, Horita J, and Ueno Y (2022) Low ^{13}C –^{13} C abundances in abiotic ethane. *Nature Communications* 13(1): 5790.

Toyoda S and Yoshida N (1999) Determination of nitrogen isotopomers of nitrous oxide on a modified isotope ratio mass spectrometer. *Analytical Chemistry* 71(20): 4711–4718.

Toyoda S, Yoshida N, and Koba K (2017) Isotopocule analysis of biologically produced nitrous oxide in various environments. *Mass Spectrometry Reviews* 36(2): 135–160.

Wang Z, Schauble EA, and Eiler JM (2004) Equilibrium thermodynamics of multiply substituted isotopologues of molecular gases. *Geochimica et Cosmochimica Acta* 68(23): 4779–4797.

Wang DT, Gruen DS, Lollar BS, Hinrichs K-U, Stewart LC, Holden JF, Hristov AN, Pohlman JW, Morrill PL, Konneke M, Delwiche KB, Reeves EP, Sutcliffe CN, Ritter DJ, Seewald JS, McIntosh JC, Hemond HF, Kubo MD, Cardace D, Hoehler TM, and Ono S (2015) Nonequilibrium clumped isotope signals in microbial methane. *Science* 348(6233): 428–431.

Wang DT, Welander PV, and Ono S (2016) Fractionation of the methane isotopologues $^{13}CH_4$, $^{12}CH_3D$, and $^{13}CH_3D$ during aerobic oxidation of methane by Methylococcus capsulatus. *Geochimica et Cosmochimica Acta* 192: 186–202.

Wang DT, Reeves EP, McDermott JM, Seewald JS, and Ono S (2018) Clumped isotopologue constraints on the origin of methane at seafloor hot springs. *Geochimica et Cosmochimica Acta* 223: 141–158.

Wang Z, Nelson DD, Dettman DL, McManus JB, Quade J, Huntington KW, Schauer AJ, and Sakai S (2020) Rapid and precise analysis of carbon dioxide clumped isotopic composition by tunable infrared laser differential spectroscopy. *Analytical Chemistry* 92(2): 2034–2042.

Weiss GM, Sessions AL, Julien M, Csernica T, Yamada K, Gilbert A, Freeman KH, and Eiler JM (2023) Analysis of intramolecular carbon isotope distributions in alanine by electrospray ionization orbitrap mass spectrometry. *International Journal of Mass Spectrometry* 493: 117128.

Whitehill AR, Joelsson LMT, Schmidt JA, Wang DT, Johnson MS, and Ono S (2017) Clumped isotope effects during OH and Cl oxidation of methane. *Geochimica et Cosmochimica Acta* 196: 307–325.

Xie H, Dong G, Formolo M, Lawson M, Liu J, Cong F, Mangenot X, Shuai Y, Ponton C, and Eiler J (2021) The evolution of intra- and inter-molecular isotope equilibria in natural gases with thermal maturation. *Geochimica et Cosmochimica Acta* 307: 22–41.

Yeung LY, Young ED, and Schauble EA (2012) Measurements of $^{18}O^{18}O$ and $^{17}O^{18}O$ in the atmosphere and the role of isotope-exchange reactions. *Journal of Geophysical Research: Atmospheres* 117(D18).

Yeung LY, Ash JL, and Young ED (2014) Rapid photochemical equilibration of isotope bond ordering in O_2. *Journal of Geophysical Research: Atmospheres* 119(17): 10552–10566.

Yeung LY, Ash JL, and Young ED (2015) Biological signatures in clumped isotopes of O_2. *Science* 348(6233): 431–434.

Yeung LY, Murray LT, Ash JL, Young ED, Boering KA, Atlas EL, Schauffler SM, Lueb RA, Langenfelds RL, Krummel PB, Steele LP, and Eastham SD (2016) Isotopic ordering in atmospheric O_2 as a tracer of ozone photochemistry and the tropical atmosphere. *Journal of Geophysical Research: Atmospheres* 121(20): 12,541–12,559.

Yeung LY, Li S, Kohl IE, Haslun JA, Ostrom NE, Hu H, Fischer TP, Schauble EA, and Young ED (2017) Extreme enrichment in atmospheric $^{15}N^{15}N$. *Science Advances* 3(11): eaao6741.

Yeung LY, Hayles JA, Hu H, Ash JL, and Sun T (2018) Scale distortion from pressure baselines as a source of inaccuracy in triple-isotope measurements. *Rapid Communications in Mass Spectrometry* 32(20): 1811–1821.

Yeung LY, Haslun JA, Ostrom NE, Sun T, Young ED, van Kessel MAHJ, Lücker S, and Jetten MSM (2019) In situ quantification of biological n2 production using naturally occurring $^{15}N^{15}N$. *Environmental Science & Technology* 53(9): 5168–5175.

Yeung LY, Murray LT, Banerjee A, Tie X, Yan Y, Atlas EL, Schauffler SM, and Boering KA (2021) Effects of ozone isotopologue formation on the clumped-isotope composition of atmospheric O_2. *Journal of Geophysical Research: Atmospheres* 126(14): e2021JD034770. 2021JD034770.

Yoshida N and Toyoda S (2000) Constraining the atmospheric n2o budget from intramolecular site preference in n2o isotopomers. *Nature* 405(6784): 330–334.

Young E (2019) A two-dimensional perspective on CH_4 isotope clumping: Distinguishing process from source. In: Orcutt BN, Daniel I, and Dasgupta R (eds.) *Deep Carbon Past to Present*, pp. 388–414. Cambridge: Cambridge University Press.

Young ED, Rumble D, Freedman P, and Mills M (2016) A large-radius high-mass-resolution multiple-collector isotope ratio mass spectrometer for analysis of rare isotopologues of O_2, N_2, CH_4 and other gases. *International Journal of Mass Spectrometry* 401: 1–10.

Young ED, Kohl ID, Sherwood Lollar B, Etiope G, Rumble D III, Li S, Haghnegahdar M, Schauble EA, McCain KA, Foustoukos DI, Sutcliffe CN, Warr O, Ballentine CJ, Onstott TC, Hosgormez H, Neubeck A, Marques JM, Perez-Rodriquez I, Rowe AR, LaRowe DE, Magnabosco C, Yeung LY, Ash JL, and Bryndzia LT (2017) The relative abundances of resolved $^{12}CH_2D_2$ and $^{13}CH_3D$ and mechanisms controlling isotopic bond ordering in abiotic and biotic methane gases. *Geochemica et Cosmochimica Acta* 203: 235–264.

Zeichner SS, Wilkes EB, Hofmann AE, Chimiak L, Sessions AL, Makarov A, and Eiler JM (2022) Methods and limitations of stable isotope measurements via direct elution of chromatographic peaks using gas chromotography-orbitrap mass spectrometry. *International Journal of Mass Spectrometry* 477: 116848.

Zeichner SS, Aponte JC, Bhattacharjee S, Dong G, Hofmann AE, Dworkin JP, Glavin DP, Elsila JE, Graham HV, Naraoka H, Takano Y, Tachibana S, Karp AT, Grice K, Holman AI, Freeman KH, Yurimoto H, Nakamura T, Noguchi T, Okazaki R, Yabuta H, Sakamoto K, Yada T, Nishimura M, Nakato A, Miyazaki A, Yogata K, Abe M, Okada T, Usui T, Yoshikawa M, Saiki T, Tanaka S, Terui F, Nakazawa S, Abe SIW, Tsuda Y, Hamase K, Fukushima K, Aoki D, Hashiguchi M, Mita H, Chikaraishi Y, Ohkouchi N, Ogawa NO, Sakai S, Parker ET, McLain HL, Orthous-Daunay F-R, Vuitton V, Wolters C, Schmitt-Kopplin P, Hertkorn N, Thissen R, Ruf A, Isa J, Oba Y, Koga T, Yoshimura T, Araoka D, Sugahara H, Furusho A, Furukawa Y, Aoki J, Kano K, Nomura SIM, Sasaki K, Sato H, Yoshikawa T, Tanaka S, Morita M, Onose M, Kabashima F, Fujishima K, Yamazaki T, Kimura Y, and Eiler JM (2023a) Polycyclic aromatic hydrocarbons in samples of ryugu formed in the interstellar medium. *Science* 382(6677): 1411–1416.

Zeichner SS, Chimiak L, Elsila JE, Sessions AL, Dworkin JP, Aponte JC, and Eiler JM (2023b) Position-specific carbon isotopes of murchison amino acids elucidate extraterrestrial abiotic organic synthesis networks. *Geochimica et Cosmochimica Acta* 355: 210–221.